An International Journal of Optimization and Control: Theories & Applications
ISSN: 2146-0957 eISSN: 2146-5703
Vol.16, No.4, pp.1319-1352 (2026)
https://doi.org/10.36922/IJOCTA026150056

RESEARCH ARTICLE

Entropy-optimized radiative Maxwell ternary nanofluid flow with magnetohydrodynamics and heat generation effects

Amir Abbas[1,2]*, Akhlaqur Rahman[3], Muhammad Farman[2,4,5], Mohamed Ahmed Hafez[6,7], Evren Hincal[2,8,9], Betty Wan Niu Voon[10], Sk. A. Shezan[11], and Naveed Ahmad[12]

[1]Department of Mathematics, Faculty of Natural Sciences and Technology, Baba Guru Nanak University, Nankana Sahib, Punjab, Pakistan

[2]Department of Mathematics, Mathematics Research Center, Near East University, Mersin 10, Nicosia, Turkey

[3]Department of Electrical Engineering and Industrial Automation, Engineering Institute of Technology, Melbourne Campus, Melbourne, Victoria, Australia

[4]Faculty of Medicine, Department of Biostatistics and Medical Informatics, Karadeniz Technical University, Trabzon, Turkey

[5]International Center for Interdisciplinary Research in Sciences, The University of Lahore, Lahore, Pakistan

[6]Faculty of Engineering and Quantity Surveying INTI International University, Nilai, Malaysia

[7]Faculty of Management, Shinawatra University, Bangtoey, Samkhok, Pathum Thani, Thailand

[8]Department of Mathematical Sciences, Saveetha School of Engineering, SIMATS, Chennai, Tamil Nadu, India

[9]Research Center of Applied Mathematics, Khazar University, Baku, Azerbaijan

[10]College of Engineering Universiti Tenaga Nasional- Kajang, Kajang, Selangor, Malaysia

[11]Department of Electrical Engineering, Prince Faisal bin Khalid bin Sultan Research Chair in Renewable Energy Studies and Applications (PFCRE), Northern Border University, Arar, Saudi Arabia

[12]Department of Chemical and Materials Engineering, College of Engineering, Northern Border University, Arar, Saudi Arabia

amir.abbas@bgnu.edu.pk; akhlaqur.rahman@eit.edu.au; muhammad.farman@neu.edu.tr; mohdahmed.hafez@newinti.edu.my; evren.hincal@neu.edu.trl; Betty@uniten.edu.my; shezan@nbu.edu.sa; naveed.ahmad@nbu.edu.sa

ARTICLE INFO

Article history:
Received: April 6, 2026
Revised: May 11, 2026
Accepted: May 13, 2026
Published Online: June 12, 2026

Keywords:
Ternary nanofluid
Entropy analysis
Porous media
Solar energy
Maxwell fluid
Heat generation
Magnetohydrodynamics

ABSTRACT

The present study investigates the mechanism of solar energy utilization as non-renewable energy in a ternary nanofluid flow and heat transfer system, incorporating a Maxwell non-Newtonian fluid over a linearly inclined stretching sheet at an inclination angle of $\pi/4$, with the effects of heat generation. The influence of a perpendicular magnetic field, which induces Lorentz forces, in a porous medium is also considered. In addition, suction at the plate and entropy generation analysis are incorporated to evaluate thermodynamic irreversibility in the system. The governing partial differential equations are transformed into a system of ordinary differential equations using appropriate similarity transformations. The transformed model is then solved using the bvp4c solver to obtain the final solution, and the results are presented in graphical and tabular form. The results indicate that increasing solar thermal radiation and magnetic field strength significantly improve temperature distribution within the system. Similarly, an increase in the heat generation parameter further enhances the temperature distribution. The presence of solar radiation enhances the fluid's thermal

*Corresponding Author

efficiency. The proposed approach presents a novel framework for improving thermal management in next-generation solar energy technologies. The magnetic force, while influencing fluid motion, also affects the system's thermal behavior. The results are compared at the end to assess the validity of the current solutions. The study further demonstrates that an increase in the Brinkman number results in a decrease in the Bejan number. Since the Bejan number represents the heat transfer irreversibility within the fluid, the increasing resistance, driven by the Brinkman number, directly affects it, thereby reducing the system's overall thermodynamic efficiency. The comparison with previously published results shows strong agreement, validating the accuracy and reliability of the present model. A sensitivity analysis is also performed to evaluate the relative influence and ranking of key governing parameters on the system response.

1. Introduction

Ternary hybrid nanofluids represent an advanced category of heat transfer fluids, created by dispersing three distinct types of nanoparticles, along with possible additives, into a base fluid. These fluids demonstrate improved thermophysical properties, such as higher thermal conductivity, optimized viscosity, and enhanced stability, compared to conventional and binary nanofluids. Owing to their superior heat transfer capabilities, they are well-suited for a wide range of energy-intensive applications. By leveraging their enhanced convective heat transfer coefficients and thermal properties, ternary nanofluids can significantly improve the efficiency of heat exchangers, cooling systems, and thermal energy storage units. Additionally, their potential in biomedical devices and electronic cooling systems underscores their versatility in developing innovative, compact thermal management solutions. The broader category of nanofluids, including mono-, hybrid-, and ternary-nanofluids, continues to expand in scope, with each type offering unique advantages tailored to specific thermal engineering challenges. **Figure 1** presents a schematic diagram of major real-time applications.

Over the past few decades, extensive research has focused on developing advanced nanofluids with enhanced thermal performance. Among these, ternary nanofluids—comprising three diverse types of nanoparticles suspended in a base fluid are more efficient thermally as compared to conventional mono nanofluids. Several studies incorporating them have shown that they are efficient thermal agents. Manjunatha *et al.*[1] presented a systematic comparative analysis and theoretical study of a ternary nanofluid past a stretching sheet to improve the thermal efficiency of the technology-based devices. Alshahrani

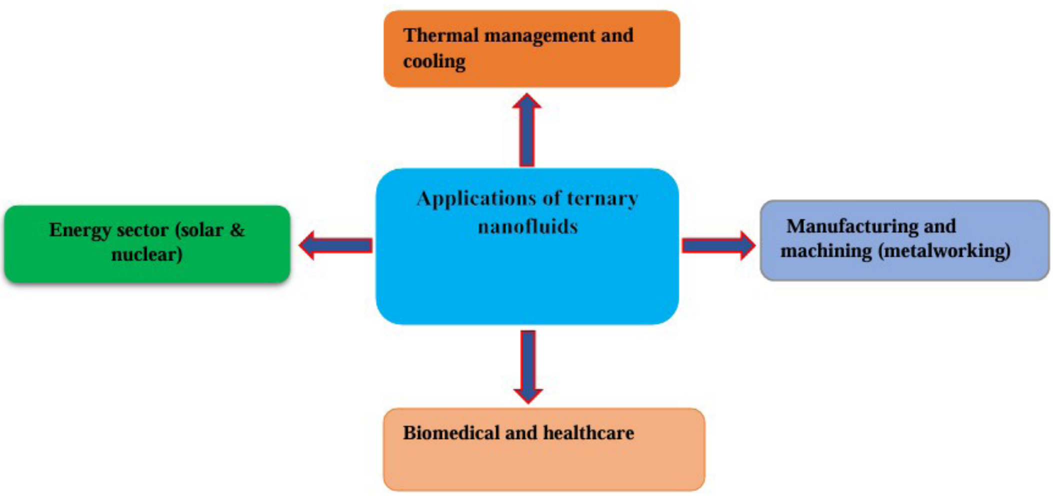

Figure 1. Applications of nanofluids

et al.[2] focused on the impact of thermal and multiple velocity-slip conditions on the ternary nanofluid flow. Adun et al.[3] analyzed a ternary nanofluid to improve the performance of a photovoltaic thermal collector. An exploration of the influence of non-linear solar radiation on the magnetohydrodynamic (MHD)-driven flow of a ternary nanofluid past a stretchable plate with couple-stress effects has also been carried out.[4] Arif et al.[5] presented a comprehensive scrutiny of unsteady flow behaviors of an incompressible water-based ternary hybrid nanofluid. Experimental results showed that hybrid nanofluids exhibited a significantly higher heat transfer rate than their unitary nanofluid counterparts. Algehyne et al.[6] employed the pseudoplastic model to explain the complex transport mechanisms governing ternary nanofluid flow across a porous stretching plate. The mechanism of fluid flow of a ternary nanofluid composed of titanium dioxide–cobalt ferrite–magnesium oxide dispersed in water past a stretchable cylinder[7] under magnetic force impact. Two novel ternary-hybrid nanoparticle combinations, integrating metal, metal oxide, and carbon components, were successfully synthesized and thoroughly characterized by Zayan et al.[8]

Priyadharshini et al.[9] focused on the optimal design and performance evaluation of a ternary nanofluid using advanced machine learning prediction. Jan et al.[10] investigated the impact of partial velocity slip and MHD on two-dimensional flow of a ternary nanofluid, comprising a polymer-based fluid with variable properties. Sajjan et al.[11] proposed studying three-dimensional flow in ternary nanofluids using the non-linear Boussinesq and Rosseland approximations with diverse shapes, densities, and thermal conductivities. Sohail et al.[12] elaborated on the mechanism of ternary nanofluids in pseudoplastic fluid passing through a permeable sheet with heat generation and utilization. Ramesh et al.[13] analyzed fluid flow and heat transfer in a ternary nanofluid over a porous slip-sheeted surface. The non-Darcy effect on ternary nanofluid flow and heat transfer processes, considering the suction impact, is examined by Faizan et al.[14] Abbas et al.[15] presented a numerical simulation of ternary nanofluid flow via the Casson fluid model, accounting for the Forchheimer number and non-equilibrium effects. The diverse types of nanofluids (mono, hybrid, and ternary nanofluids) are outlined in **Figure 2**.

A porous medium is a material that contains pores or voids, allowing fluids to flow through it. The pores can be interconnected, forming a network that enables fluid flow. Porous media have broad applications across diverse disciplines, including engineering, physics, biology, and medicine. Specifically, it plays a vital role in heat transfer systems, for example, heat exchangers, insulation, and thermal energy storage, as well as in fluid flow applications, including filtration, separation, and flow control. Farouk and Shayer[16] presented a numerical evaluation of heat transfer and fluid flow past a heated cylinder with porosity influence. Hossain et al.[17] proposed an investigation into the influence of the Forchheimer number on a vertical porous cylinder embedded in porous media. Pop and Na[18] analyzed the time-independent convection process past a hollow, slender cylinder penetrated in a porous medium. Ullah et al.[19] discussed the phenomenon of solar radiative heat transfer in a second-grade nanofluid with variable thermal conductivity and slip condition on the flat plate. Salih et al.[20] explored the mechanism of solar radiation effects on the Williamson nanofluid flow with oscillatory impact on the gasketed-plate heat exchanger embedded in the porous medium incorporating the exothermic chemical reaction. Riaz et al.[21] explored solitary wave solutions of the Sawada–Kotera equation using an efficient analytical method. Syed et al.[22] conducted computational fluid dynamics analysis and heat transfer coefficient calculations in a concentric tube heat exchanger. Maatki et al.[23] studied the time-dependent three-dimensional flow around rotating discs, accounting for fluctuations and thermal radiation.

Solar radiation is a fundamental energy source that drives many fluid dynamics processes on Earth. The sun's radiation, primarily in the form of visible light, infrared, and ultraviolet energy, interacts with the Earth's surface and atmosphere, generating temperature differences that influence fluid behavior. In fluid dynamics, solar radiation is crucial in the study of heat transfer, convection, and the formation of atmospheric and oceanic currents. The absorption and redistribution of solar energy by fluids lead to varying densities, which, in turn, drive flow patterns and turbulence. Understanding the role of solar radiation is essential for modeling natural systems such as weather patterns and ocean currents, as well as man-made systems in which temperature gradients affect fluid flow. Solar radiation also plays a key role in heating, with solar thermal systems used to warm water and buildings. In agriculture, it fuels photosynthesis, enabling plant growth, while solar greenhouses

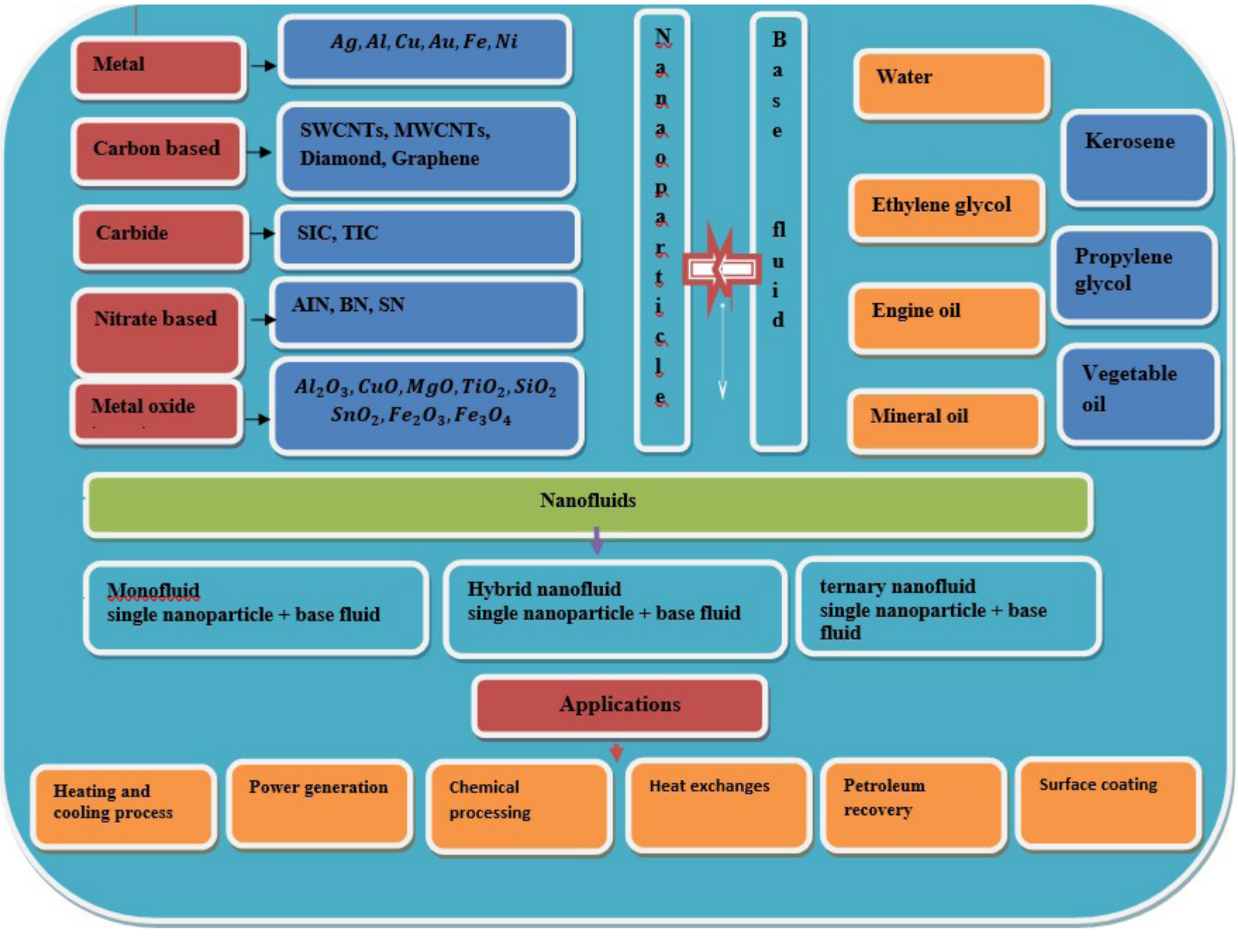

Figure 2. Ternary-hybrid–nanofluid model

Abbreviations: Ag: Silver; Al: Aluminum; Al_2O_3: Aluminum oxide; AIN: Aluminum Nitride; Au: Gold; BN: Boron nitride; Cu: Copper; CuO: Copper (II) oxide; Fe: Iron; Fe_2O_3: Iron (III) oxide; Fe_3O_4: Magnetite; MgO: Magnesium oxide; MWCNTs: Multi-walled carbon nanotubes; Ni: Nickel; SIC: Silicon carbide; SiO_2: Silicon dioxide; SN: Silicon nitride; SnO_2: Tin dioxide; SWCNTs: Single-walled carbon nanotubes; TIC: Titanium carbide; TiO_2: Titanium dioxide.

optimize sunlight for extended growing seasons.

Additionally, solar energy powers space missions through satellite panels, purifies water through solar desalination, and can even be used in solar cookers and dryers, offering efficient, eco-friendly alternatives to traditional methods. This research seeks to explore the mechanisms through which solar radiation influences fluid motion and how these interactions can be applied to improve our understanding of complex fluid systems. The industrial importance of solar radiation has led to a wealth of research and publications on the topic. Examinations were performed for natural convection over a vertical flat surface, with solar radiation accounted for media's porosity, as reported by Chamkha.[24] Mahendran *et al.*[25] observed the effect of the nanoparticle, titanium dioxide, on the *Haematococcus pluvialis* biomass concentration. Ghasemi *et al.*[26] conducted a scientific investigation to examine the influence of solar radiation on MHD-driven nanofluid flow over a stretched plate, revealing a significant increase in temperature when thermophoretic effects and Brownian motion are simultaneously enhanced. Chen *et al.*[27] presented a comprehensive heat transfer past the solar receiver to maximize its performance. Pustovalov[28] examined the optical properties of nanoparticles and nanofluids for efficient absorption of solar radiation and heating. Obalalu *et al.*[29] provided a theoretical and numerical study of time-dependent two-dimensional MHD-driven squeezing flow driven by non-Newtonian fluid under the sun's radiation. Aziz *et al.*[30] investigated the impact of nanoparticles on conventional pit and fissure sealants. Khan and Pop[31] focused on the mechanism of boundary-layer flow of a nanofluid over the stretching surface. Rauf *et al.*[32] discussed the processes of fluid flow and heat transfer in Maxwell hybrid nanofluid with thermal diffusion, diffusion-thermo effects, and nanoparticle shape parameter effects. The fluid flow and energy transmission processes along a porous stretching sheet with slip boundary conditions are examined by Varatharaj *et al.*,[33] and Devi *et al.*[34] studied hybrid nanofluid flow on a porous plate. In addition, a ternary nanofluid on the moving plate was studied.[35] Aich *et al.*[36] discussed the matter of the impact of the chemical reaction and inclined magnetic field on the flow of Maxwell hybrid nanofluid over the moving needle fixed in the non-Darcy media. Jameel *et al.*[37] elaborated the entropy generation process for Darcy–Forchheimer Maxwell nanofluid flow along a porous stretching sheet, accounting for a generalized heat transfer law and Joule heating. Amudhini *et al.*[38] conducted an analysis of entropy generation for a tetra-hybrid non-Newtonian fluid flow with thermal radiation and Soret–Dufour effects over a porous inclined stretching sheet. Novel MHD and entropy generation analysis of radiative nanofluid flow using an artificial neural network approach has been analyzed by Razzaq *et al.*[39] The novelty of this work lies in the unified modeling of Maxwell ternary nanofluid flow by simultaneously incorporating Lorentz force, heat generation, solar radiation, porous media, and entropy generation over a permeable linearly stretching sheet. The results provide useful insights for thermal management and cooling system applications.

2. Mathematical modeling

Following previous works,[33-37] the flow equations are formulated under the assumptions of a viscous, incompressible, and steady viscoelastic fluid flow of a Maxwell fluid. A ternary nanofluid based on silver–titania–alumina (Ag–TiO_2–Al_2O_3) is considered. The surface is inclined at the $\alpha = \pi/4$. The effects of buoyancy and heat generation, along with the combined influence of the magnetic force and solar radiation on the surface, are taken into account. The flow configuration is shown in **Figure 3**.

The flow equations are as follows:

$$\frac{\partial u}{\partial x} + \frac{\partial v}{\partial y} = 0 \tag{1}$$

$$\left(u\frac{\partial u}{\partial x} + v\frac{\partial u}{\partial y} \right) = \frac{\mu_{thnf}}{\rho_{thnf}}\frac{\partial^2 u}{\partial y^2} - \beta_1\left(u^2\frac{\partial^2 u}{\partial x^2} + v^2\frac{\partial^2 u}{\partial y^2} + 2uv\frac{\partial^2 u}{\partial x \partial y} \right) - \frac{g\left(\rho\beta_T\right)_{hnhnf}}{\rho_{thnf}}\left(T - T_\infty\right)Cos\left(\alpha\right) \tag{2}$$

$$u\frac{\partial T}{\partial x} + v\frac{\partial T}{\partial y} = \frac{k_f}{\left(\rho C_p\right)_f} \tag{3}$$

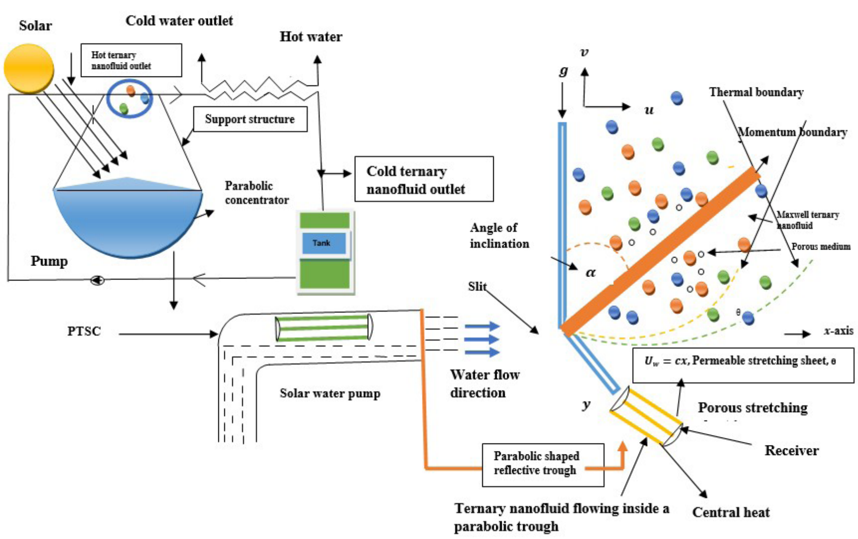

Figure 3. Flow structure of a ternary nanofluid system
Abbreviation: PTSC: Parabolic trough solar collector.

$$\left[\frac{\frac{k_{thnf}}{k_f}}{\frac{(\rho C_p)_{thnf}}{(\rho C_p)_f}}+\frac{4.4T_\infty^3\sigma}{3\frac{(\rho C_p)_{thnf}}{(\rho C_p)_f}k_fK_R}\right]\frac{\partial^2 T}{\partial y^2}+\frac{Q_o}{(\rho C_p)_{thnf}}(T-T_\infty)$$

Imposed boundary conditions (BCs).

$$\left.\begin{aligned}&u=U_w(x)=cx,\ v=-v_o\\&T=T_w\ \ C=C_w\ at\ y=0\\&u\to 0,T\to T_\infty,C\to C_\infty.\end{aligned}\right\}\tag{4}$$

The symbols and notations appearing in the current equations are shown in **Table 1**.

2.1. Engineering parameters

The key physical parameters of interest are the skin friction coefficient and the Nusselt number, defined as:

$$\left.\begin{aligned}&C_f=\frac{\mu_{hnf}}{\rho_f U_W^2}\left(\frac{\partial u}{\partial y}-\beta_1\left(2\tilde{u}\tilde{v}\frac{\partial^2 u}{\partial x\partial y}+v^2\frac{\partial^2 u}{\partial y^2}\right)\right)_{y=0}\\&Nu_x=-\frac{xk_{hnf}}{k_f(T_o-T_\infty)}\left(\frac{4.4T_\infty^3\sigma}{3\frac{(\rho C_p)_{thnf}}{(\rho C_p)_f}k_fK_R}+\frac{\partial T}{\partial y}\right)_{y=0}\end{aligned}\right\}\tag{5}$$

2.2. Entropy generation analysis

Following a previous work,[37] the entropy generation (EG) can be formulated as:

$$\begin{aligned}E_G=&\underbrace{\frac{k_f}{T_\infty^2}\left(\frac{k_{thnf}}{k_f}+\frac{16T_\infty^3\sigma}{(\rho C_p)_{thnf}3K_R}\right)\left(\frac{\partial T}{\partial y}\right)^2}_{Thermal\ irreversibility}\\&+\underbrace{\frac{\mu_{thnf}}{k_1T_\infty}u^2+\frac{\mu_{thnf}}{T_\infty}\left(\frac{\partial u}{\partial y}\right)^2}_{Fluid\ friction\ irreversibility}\\&+\underbrace{\frac{\beta_1\mu_{thnf}}{T_\infty}\left(u\frac{\partial^2 u}{\partial y^2}\right)^2}_{Maxwell\ viscoelastic\ irreversibility}\\&+\underbrace{\frac{\sigma_{thnf}B_o^2}{T_\infty}u^2}_{Joule\ description}\end{aligned}\tag{6}$$

3. Solutions mythology

In this section, the entire solution method is explained. **Equations 1–4** are transformed into ordinary differential equations utilizing suitable transformation variables given in the next subsection.

3.1. Similarity variable formulation

The conversion from partial differential **Equations 1–3**, along with boundary conditions (**Equation 4**), is performed using the similarity formulation in the form of stream function formulation variables given in **Equation 7**.[6]

$$\left.\begin{aligned}&u=cxf'(\eta),v=\sqrt{cv_f}f(\eta)\\&\theta(\eta)=\frac{T-T_\infty}{T_o-T_\infty},\eta=\sqrt{\frac{c}{v_f}}y\end{aligned}\right\}\tag{7}$$

Utilizing the similarity variables given in **Equation 5**, following the approach of Khan and Pop,[31] within **Equations 1–4** leads to the automatic satisfaction of the continuity equation, while the other equations are reduced in the following:

$$\begin{aligned}&\frac{E_1}{E_2}f'''-f'^2-ff''-\lambda_1\left(f^2f'''-2ff'f''\right)\\&-\frac{E_3}{E_2}\lambda\theta\mathrm{Cos}(\alpha)-\frac{E_4}{E_2}Mf'-\frac{E_1}{E_2}Kf'=0\end{aligned}\tag{8}$$

$$\left(\frac{E_5}{E_6}+\frac{4}{3E_6}Rd\right)\frac{1}{Pr}\theta''+\frac{1}{E_6}Q\theta+f\theta'=0\tag{9}$$

BCs

$$\left.\begin{aligned}&f=S,f'=1,\theta=1,\mathrm{at}\,\eta=0\\&f'\to 0,\theta\to 0,\mathrm{as}\,\eta\to\infty\end{aligned}\right\}\tag{10}$$

Here, $E_1=\frac{\mu_{thnf}}{\mu_f},E_2=\frac{\rho_{thnf}}{\rho_f},E_3=\frac{(\rho\beta_T)_{thnf}}{(\rho\beta_T)_f},$

$E_4=\frac{\sigma_{htnf}}{\sigma_f},E_5=\frac{k_{hnf}}{k_f},E_6=\frac{(\rho C_P)_{thnf}}{(\rho C_P)_f}$

The symbols and definitions of the pertinent parameters are presented in **Table 2**.

Substituting **Equation 7** into **Equation 5** and carrying out some algebraic manipulations, the following transformed engineering quantities are obtained:

Table 1. The mathematical reporting of the parameter appearing in the equations

Notation	Definition	Notation	Definition
(x, y)	Horizontal and vertical coordinates	$(C_P)_f$	Base fluid specific heat
μ_f	Base fluid dynamics viscosity	σ_f	Base fluid electrical conductivity
ν_f	Base fluid kinematic viscosity	$(\beta_T)_f$	Base fluid thermal expansion coefficient due to temperature
ρ_f	Base fluid density	ρ_{thnf},	Ternary nanofluid density
k_f	Base fluid thermal conductivity	k_{thnf}	Ternary nanofluid thermal conductivity
μ_{thnf}	Ternary nanofluid fluid dynamics viscosity	$(C_P)_{hnf}$	Specific heat of the ternary nanofluid
ν_{thnf}	Ternary nanofluid fluid kinematic viscosity	σ_{hnf}	Ternary nanofluid electrical conductivity
β	Relaxation constant time	g	Gravity force
B_o^2	Magnetic field strength	K_o	Porosity constant
K_R	Absorption coefficient	σ	Stefan–Boltzmann constant
$q_r = -\dfrac{16T_\infty^3\sigma}{3K_R}\dfrac{\partial T}{\partial y}.$	Roseland approximation	u, v	Horizontal and vertical velocity components
T_w	Temperature at the plate	T_∞	Temperature in the free stream
U_w	Stretching sheet velocity	c	Stretching rate constant
v_o	Sheet permeability constant	$(\beta_T)_{thnf}$	Ternary nanofluid thermal expansion coefficient due to temperature
$\alpha_m = \dfrac{k_f}{(\rho C_P)_f}$	Thermal diffusivity	α	Angle of inclination
Taylor series of T^4	$\mathrm{T}^4 \approx 4\mathrm{T}_\infty^3\mathrm{T} - 3\mathrm{T}_\infty^4.$	Q_o	Volumetric flow rate

$$\left.\begin{aligned} Re_x^{1/2}C_f &= \frac{\mu_{hnf}}{\mu_f}\left((f''(0) - \lambda_1 f^2(0) f''(0) - 2f(0)f'(0)\right) \\ Re_x^{-1/2}Nu_x &= -\frac{k_{hnf}}{k_f}\left((1+Rd)\theta'(0)\right) \end{aligned}\right\} \quad (11)$$

The thermophysical properties of the ternary nanofluids are shown in **Table 3**. The experimental thermophysical property formula for ternary nanofluids is given in **Table 4**.

Here, φ_1, φ_2 and ϕ_3 represent the volume fractions of solid nanoparticles, Ag, TiO_2, and Al_2O_3 respectively. The subscripts $1, s_1, s_2$ and s_3 are used to distinguish the thermo–physical properties of the base fluid, the first-type nanoparticles (Ag), the second-type nanoparticles (TiO_2), and the third-type nanoparticles (Al_2O_3)

Table 2. The symbols and definitions of the pertinent parameters

Parameters	**Definition**	**Dimension**
$Rd=\frac{k_f K_R}{4\sigma^* T_\infty^3}$	Radiation parameter	$\frac{\left[\frac{ML}{T^3K}\right]\left[L^{-1}\right]}{\left[\frac{M}{T^3K4}\right]\left[K^3\right]}=1$
$\lambda_1=\beta_1 c$	Maxwell fluid parameter	$\left[T\right]\left[T^{-1}\right]=1$
$\lambda=\frac{g\left(\beta_T\right)_f \Delta T}{c^2 x}$	Buoyancy parameter	$\frac{\left[LT^{-2}\right]\left[K^{-1}\right]\left[K\right]}{\left[T^{-2}\right]\left[L\right]}=1$
$M=\frac{\sigma_f B_o^2}{c\rho_f}$	Magnetic field parameter	$\frac{\left[M^{-1}L^{-3}T^3A^2\right]\left[M^2T^{-4}A^{-2}\right]}{\left[T^{-1}\right]\left[ML^{-3}\right]}=1$
$K=\frac{\nu_f}{K_o c}$	Dimensionless porosity parameter	$\frac{\left[L^2T^{-1}\right]}{\left[L^2\right]\left[T^{-1}\right]}=1$
$Pr=\frac{\nu_f}{\alpha_f}$	Prandtl number	$\frac{\left[L^2T^{-1}\right]}{\left[L^2T^{-1}\right]}=1$
$Q=\frac{Q_o}{c\left(\rho C_p\right)_{thnf}}$	Heat generation parameter	$\frac{\left[ML^{-1}T^{-3}K^{-1}\right]}{\left[ML^{-1}T^{-3}K^{-1}\right]}$
$S=\frac{v_o}{\sqrt{c\nu_f}}\left(v_o>0\right)$	Suction parameter	$\frac{\left[LT^{-1}\right]}{\sqrt{T^{-1}L^2L^{-1}}=\left[LT^{-1}\right]}=1$
$\eta=\sqrt{\frac{c}{\nu_f}}y$	Variable of similarity	$\sqrt{\frac{T^{-1}}{L^2T^{-1}}}L=1$
Prime notation '	Derivative w.r.t. η.	
$Re_x^{1/2}C_f$	Skin friction coefficient	$\frac{\left[LT^{-1}\right]\left[L\right]\left[ML^{-1}T^{-2}\right]}{\left[L^2\right]\left[T^{-1}\right]\left[ML^{-1}T^{-2}\right]}=1$
$Re_x^{-1/2}Nu_x=\left(\frac{U_w x}{\nu_f}\right)\frac{(h)(x)}{k_f}$	Nusselt number	$\frac{[1]\left[MT^{-3}K^{-1}\right]\left[L\right]}{\left[MT^{-3}K^{-1}L\right]}=1$
$Re_x=\frac{U_w x}{\nu_f}$	Local Reynolds number	$\frac{\left[LT^{-1}\right]\left[L\right]}{\left[L^2\right]\left[T^{-1}\right]}=1$
α	Angle of inclination	$\left[\frac{L}{L}\right]$

, respectively.

Using **Equation 7**, **Equation 6** takes the following[37] dimensionless form of e N_G derived as:

$$N_G = \alpha_1 \left(\frac{k_{\mathrm{thnf}}}{k_f} + \frac{4}{3} Rd \right) \theta' + \frac{\mu_{thnf}}{\mu_f} Br \left[\left(\frac{1}{\alpha_1} K \right) f' + f''^2 \right] + \frac{\mu_{thnf}}{\mu_f} Br \lambda_1 \left(f' \right)^2 \left(f''' \right)^2 + \frac{\sigma_{thn}}{\sigma_f} MBrf'^2 \quad (12)$$

$$Be = \frac{\left(\frac{k_{\mathrm{thnf}}}{k_f} + \frac{4}{3} Rd \right) \theta'}{N_G} \quad (13)$$

The pertinent parameters of the physical significance appearing in **Equations 12 and 13** are explained in **Table 5** with their accurate formulae.

It is important to note that Be lies within the range $[0\ 1]$. For $Be \ll \frac{1}{2}$, entropy generation

Table 3. Thermophysical properties of the ternary nanofluid[33]

Properties	$\rho \left(\frac{\mathbf{Kg}}{\mathbf{m}} \right)$	$\mathbf{C_p}$ ($\mathbf{JKg^{-1}K^{-1}}$	$\mathbf{k} \left(\mathbf{Wm^{-1}K^{-1}} \right)$	σ (s/m)	$\beta \times 10^{-5}\,\mathbf{K}^{-1}$
	997.1	4,179	0.613	5.5×10^{-6}	2.1×10^{-4}
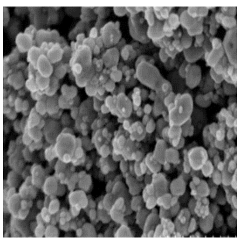	10,500	235	429	6.7×10^{7}	1.89×10^{-5}
	4,250	686.2	8.95	2.83×10^{6}	0.9×10^{-5}
	3,970	765	40	3.5×10^{6}	0.85×10^{-5}

Table 4. Correlations of thermophysical properties for ternary-hybrid nanofluids used in a previous work[33]

Properties	Ternary nanofluid ($\tau\eta\nu\phi$) and hybrid nanofluid (hnf)
Density	$\rho_{thnf}=(1-\phi_3)\left\{(1-\phi_2)\left[(1-\phi_1)\rho_f+\phi_1\rho_{s1}\right]+\phi_2\rho_{s2}\right\}+\phi_3\rho_{s3}$ $\rho_{hnf}=(1-\phi_2)\left[(1-\phi_1)\rho_f+\phi_1\rho_{s1}\right]+\phi_2\rho_{s2}$
Heat capacity	$(\rho C_p)_{thnf}=(1-\phi_3)\left\{(1-\phi_2)\left[(1-\phi_1)(\rho C_p)_f+\phi_1(\rho C_p)_{s1}\right]+\phi_2(\rho C_p)_{s2}\right\}+\phi_3(\rho C_p)_{s3}$ $(\rho C_p)_{hnf}=(1-\phi_2)\left[(1-\phi_1)(\rho C_p)_f+\phi_1(\rho C_p)_{s1}\right]+\phi_2(\rho C_p)_{s2}$
Dynamic viscosity	$\frac{\mu_{thnf}}{\mu_f}=\frac{1}{(1-\phi_1)^{2.5}(1-\phi_2)^{2.5}(1-\phi_3)^{2.5}}$ $\frac{\mu_{hnf}}{\mu_f}=\frac{1}{(1-\phi_1)^{2.5}(1-\phi_2)^{2.5}}$
Thermal conductivity	$\frac{k_{thnf}}{k_{hnf}}=\left[\frac{k_{s3}+2k_{hnf}-2\phi_3(k_{hnf}-k_{s3})}{k_{s3}+2k_{hnf}+\phi_3(k_{hnf}-k_{s3})}\right]$ where $\frac{k_{hnf}}{k_{nf}}=\left[\frac{k_{s2}+2k_{nf}-2\phi_2(k_{nf}-k_{s2})}{k_{s2}+2k_{nf}+\phi_2(k_{nf}-k_{s2})}\right]$ $\frac{k_{nf}}{k_f}=\left[\frac{k_{s1}+2k_f-2\phi_1(k_f-k_{s1})}{k_{s1}+2k_f+\phi_1(k_f-k_{s1})}\right]$
Electrical conductivity	$\frac{\sigma_{thnf}}{\sigma_{hnf}}=\left[\frac{\sigma_{s3}+2\sigma_{hnf}-2\phi_3(\sigma_{hnf}-\sigma_{s3})}{\sigma_{s3}+2\sigma_{hnf}+\phi_3(\sigma_{hnf}-\sigma_{s3})}\right]$ where $\frac{\sigma_{hnf}}{\sigma_{nf}}=\left[\frac{\sigma_{s2}+2\sigma_{nf}-2\phi_2(\sigma_{nf}-\sigma_{s2})}{\sigma_{s2}+2\sigma_{nf}+\phi_2(\sigma_{nf}-\sigma_{s2})}\right]$ $\frac{\sigma_{nf}}{\sigma_f}=\left[\frac{\sigma_{s1}+2\sigma_f-2\phi_1(\sigma_f-\sigma_{s1})}{\sigma_{s1}+2\sigma_f+\phi_1(\sigma_f-\sigma_{s1})}\right]$

due to heat transfer irreversibility is significantly lower than that resulting from frictional effects. Conversely, when $Be \gg \frac{1}{2}$, entropy production from frictional irreversibility becomes negligible compared to that caused by heat transfer. At $Be = \frac{1}{2}$, both mechanisms contribute equally to entropy generation.

3.2. Solution of the problem by finite difference-based solver bvp4c

Solutions of ordinary differential equations are computed using the finite difference-based solver bvp4c, which is built on the discretization process of the finite difference method for accurate numerical solutions.

Table 5. The definition of the parameters appearing in Equations 12 and 13

Notations of the parameters	Definition	Dimension
$\alpha_1 = \frac{\Delta T}{T_\infty}$	Dimensionless temperature ratio variable	$\left[\frac{K}{K}\right]$
$N_G = \frac{E_G T_\infty v_f}{k_f C \Delta T}$	Total Entropy generation	$\frac{[ML^{-1}T^{-3}K^{-1}][K][L^2T^{-1}]}{[MLT^{-3}K^{-1}][T^{-1}][K]}$
$Br = PrEc = \frac{\mu_f c^2 x^2}{k_f \Delta T}$	Brinkman number	$\frac{[ML^{-1}T^{-1}][T^{-2}][L^2]}{[MLT^{-3}K^{-1}][K]} = 1$
$Pr = \frac{v_f}{\alpha_f}$	Prandtl number	$\frac{[L^2T^{-1}]}{[L^2T^{-1}]} = 1$
$Ec = \frac{(cx)^2}{C_P \Delta T}$	Eckert number	$\frac{[T^{-1}L]^2}{[L^2T^{-2}K^{-1}][K]} = 1$
$Be = \frac{\left(\frac{k_{thnf}}{k_f} + \frac{4}{3}Rd\right)\theta'}{N_G}$	Bejan number	$\frac{\left[\frac{WL^{-1}K^{-1}}{WL^{-1}K^{-1}} + \frac{4}{3}(1)\right][1]}{1} = 1$
$M = \frac{\sigma_f B_o^2}{c\rho_f}$	Magnetic field parameter	$\frac{[A^2T^3M^{-1}L^{-3}][M^2T^{-4}A^{-2}]}{[T^{-1}][ML^{-3}]} = 1$

3.2.1. bvp4c solver

The system of ordinary differential **Equations 8–13** is solved by MATLAB bvp4c. The numerical solutions of the velocity field and temperature field, along with the skin friction coefficient and Nusselt number.

These equations are further progressed as follows:

$$f = P(1), f' = P(2), f'' = P(3), \theta = P(4), \quad \theta' = P(5) \tag{14}$$

Putting the above in the equations, we have the following:

$$PP1 = -\Big(-P(2)^2 - P(1)P(2) - \lambda_1(-2P(1)P(2)P(3)) - \frac{E_3}{E_2}\lambda P(4)\mathrm{Cos}(\alpha) - \frac{E_4}{E_2}MP(2) - \frac{E_1}{E_2}KP(2)\Big)) \Big/ \left(\frac{E_1}{E2} + \lambda_1 P(1)\right) \tag{15}$$

$$PP2 = -\frac{P(1)P(5)}{\left(\frac{E_5}{E_6} + \frac{4}{3E_6}Rd\right)\frac{1}{Pr}} - \frac{1}{E_6\left(\frac{E_5}{E_6} + \frac{4}{E_6}Rd\right)\frac{1}{Pr}}QP(4) \tag{16}$$

BCs

$$\left.\begin{matrix} P(1) = S, P(2) = 1, P(4) = 1, \text{at}\,\eta = 0 \\ P(2) \to 0, P(4) \to 0, \text{as}\,\eta \to \infty. \end{matrix}\right\} \tag{17}$$

The above system of first-order differential equations is inserted into the MATLAB bvp4c solver for the final solution. The obtained solutions are portrayed in graphs and tables. The obtained solutions are placed at their appropriate place in the manuscript. The iteration process continues at each position until the convergence criterion for all variables 10^{-15}, is met, and the boundary condition is satisfied at the surface and asymptotically far from the surface. The convergence criteria for f', θ, at each step, using a 20 by 20 mesh size, are defined as:

$$max|f'| + max|f| + max|\theta| \leq 10^{-5} \tag{18}$$

The start of the iteration is $\eta = 0$ and walks down implicitly, and the maximum value of $\eta_\infty = 5$. According to the convergence criteria given in **Equation 18** and the boundary conditions given in **Equation 18**, it is evident that solutions satisfy the given boundary conditions. The solutions show a remarkable asymptotic behavior. Moreover, the solutions exhibit pronounced asymptotic behavior as the distance from the surface increases, confirming that the boundary conditions are effectively satisfied within the computational domain and the specified mesh size. The CPU takes approximately 20 seconds to complete a single loop over three different values of a single parameter, indicating the computational efficiency of the implemented numerical scheme.

The entire solution technique is presented as follows: The built-in bvp4c in MATLAB, a member of the finite difference scheme, is shown in **Figure 4**. This figure presents the entire model formulation and solution methodology used to obtain the final solution.

4. Results and discussion

In this section, numerical results in the form of graphs and tables are portrayed and discussed with physical reasoning.

4.1. Streamlines and isotherms for distinct values of the magnetic field parameter

In this sub-section, the streamlines and isotherms for the Maxwell ternary nanofluid are presented to aid the reader's understanding of the flow pattern, along with temperature contour plots. The impact of the magnetic number M on streamlines of Maxwell ternary nanofluid is shown in **Figures 5** and **6**. It is observed that for $M = 5.1$, the streamline pattern shows a higher magnitude away from the surface upper streamlines, while a lower magnitude occurs near the surface, as indicated by the blue region. In **Figure 6**, when $M = 6.1$, the overall magnitudes of the streamlines are obtained. As M increases, the retardation force enhances the resistance to fluid flow, resulting in a reduction of streamline values. A similar pattern is observed, with the maximum magnitude region appearing in the yellow zone. **Figures 7** and **8** illustrate the contour plot (isotherms) of the Maxwell ternary nanofluid for different values of $M = 5.1 - 6.1$, respectively. The isotherm in **Figure 7** for $M = 5.1$ shows that the maximum values occur near the surface, while the minimum values are observed away from the surface. When $M = 6.1$ is applied, the overall isotherm results indicate an enhancement in the values. The maximum values remain near the heated surface, while the lowest magnitude occurs away from the surface, as shown in **Figure 8**.

4.2. Velocity and temperature fields for distinct values of pertinent parameters

In this subsection, the numerical investigation of the ternary non-Newtonian fluid model is presented, with a focus on the physical interpretation of the results. The discussion centers around the velocity distribution f', temperature distribution θ, skin friction coefficient $Re^{1/2}C_f$, and Nusselt number $Re^{-1/2}Nu$, highlighting the influence of several critical parameters. These include the volume fractions ϕ_1, ϕ_2, ϕ_3 of the nanoparticles (Ag, TiO_2, and Al_2O_3), the heat generation parameter Q, the solar radiation parameter Rd, the magnetic field parameter MMM, the buoyancy parameter λ, the Maxwell parameter λ_1, the porosity parameter K, and the Prandtl number Pr.

Figures 9 and **10** represent the graphical outcomes of velocity f' and temperature θ for various values of nanoparticles volume fractions for ϕ_1, ϕ_2, ϕ_3, corresponding to Ag, TiO_2, and Al_2O_3, respectively. **Figure 9** shows that increasing the nanoparticle volume fractions ϕ_1, ϕ_2, ϕ_3 leads to a reduction in the velocity profile f'. Physically, this behavior occurs because a higher concentration of nanoparticles increases the fluid's effective viscosity, thereby increasing resistance and retarding fluid motion. **Figure 10** demonstrates that an increase in ϕ_1, ϕ_2, ϕ_3 enhances the temperature distribution. This is attributed to the improved thermal performance of the nanofluid caused by the higher nanoparticle

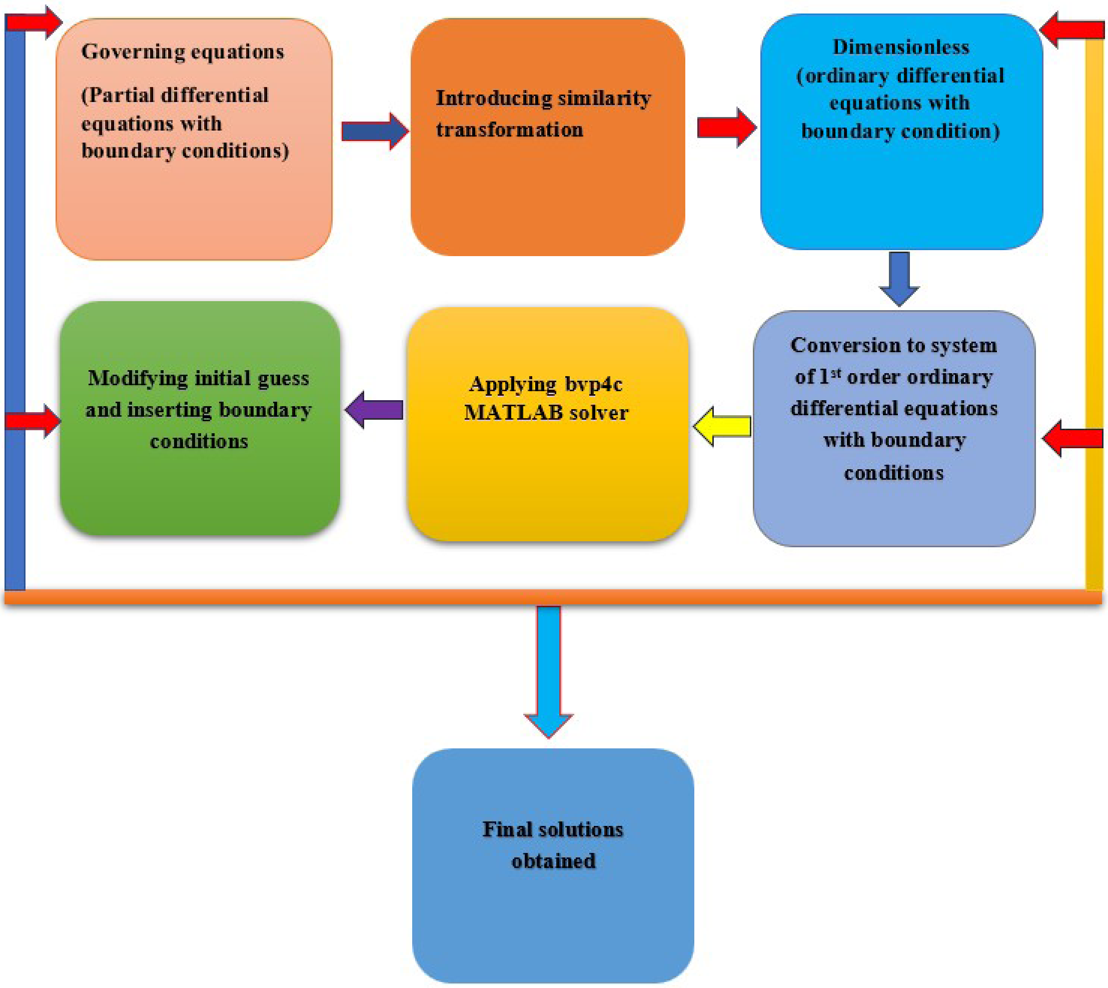

Figure 4. Solution technique schematic diagram

loading, which elevates the temperature field. **Figures 11** and **12** depict the influence of magnetic force on velocity and temperature for simple nanofluid Ag /water, hybrid nanofluid $Ag-TiO_2$ /water, and the ternary nanofluid $Ag-TiO_2-Al_2O_3$ /water. **Figure 11** depicts that the velocity magnitude decreases as M increases. This occurs because an increase in M strengthens the Lorentz force acting normal to the flow direction, which opposes the motion and attenuates the velocity field for all considered nanofluids. **Figure 12** presents the effect of M on θ, revealing that temperature increases as M rises. This behavior arises because the intensified Lorentz force increases Joule heating, raising the temperature. The effects of Maxwell fluid parameter λ_1 on f' and θ for all three nanofluid cases are illustrated in **Figures 13** and **14**. The velocity field f' shows a decreasing trend in response to the increasing magnitude of λ_1. The completely opposite trend is noted in the temperature field θ under the same variations of λ_1 (**Figure 8**). Notably, the lowest velocity values are observed for the ternary nanofluid $Ag-TiO_2-Al_2O_3$ /water, while the highest values correspond to mono nanofluid Ag /water (**Figure 7**). Conversely, for the temperature field, the peak values are attained by the $Ag-TiO_2-Al_2O_3$ /water whereas the lowest magnitude is retained by the Ag /water. The impact λ on f' and θ is highlighted in the **Figures 15** and **16**, respectively. **Figure 15** shows that increasing λ results in a reduction in f', while **Figure 16** shows that the temperature profile behaves oppositely. For f', the lowest value is associated with the ternary nanofluid $Ag-TiO_2-Al_2O_3$ / water, whereas the maximum values are obtained for nanofluid Ag / water. In contrast, the temperature field exhibits a completely reversed trend. **Figures 17** and **18** present the effect of the porosity parameter K on f' and θ. The

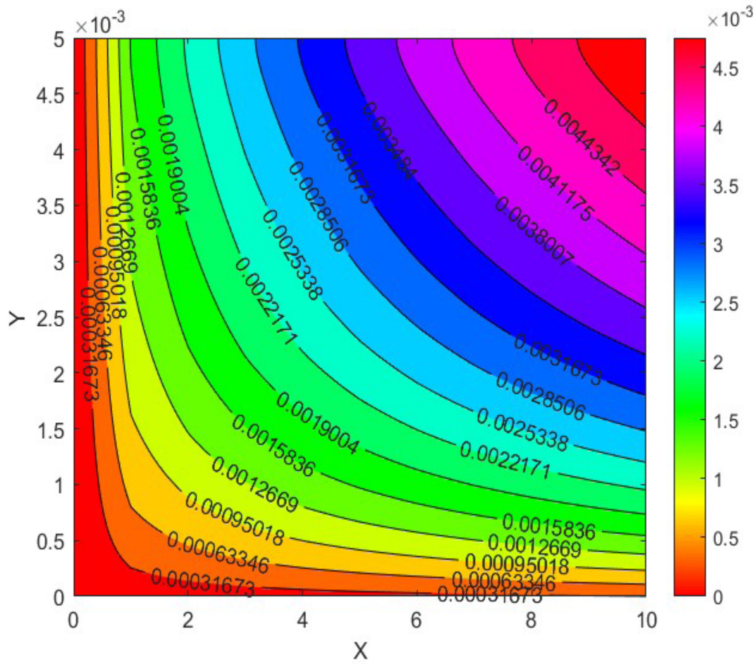

Figure 5. Streamlines of Maxwell ternary nanofluid for $M = 0.1$ at $\alpha = \frac{\pi}{4}$

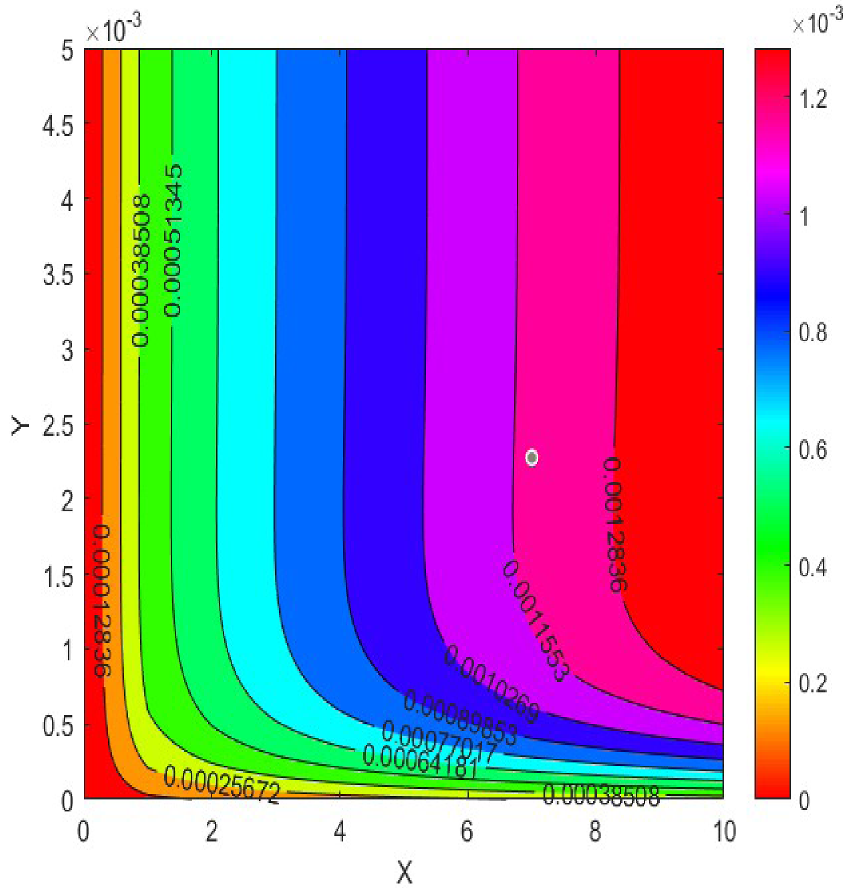

Figure 6. Streamlines of Maxwell ternary nanofluid for $M = 3.1$ at $\alpha = \frac{\pi}{4}$

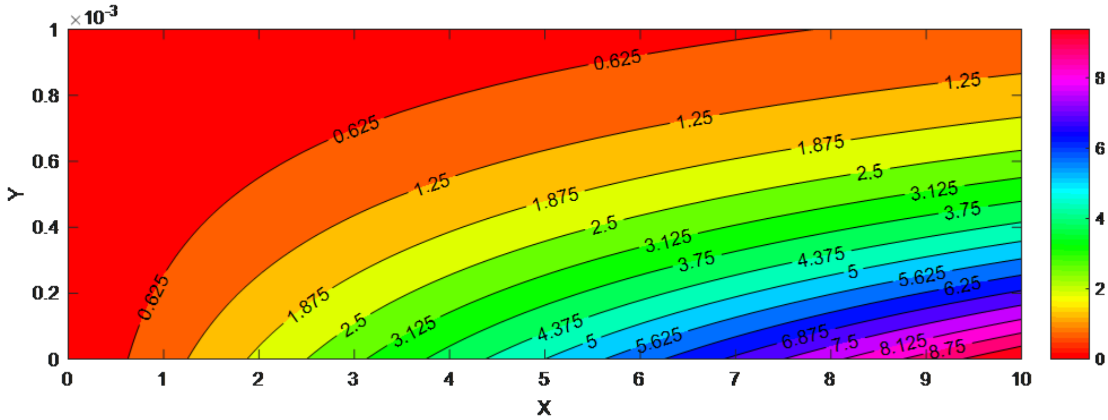

Figure 7. Isotherm of Maxwell ternary nanofluid for $M = 0.1$ at $\alpha = \frac{\pi}{4}$

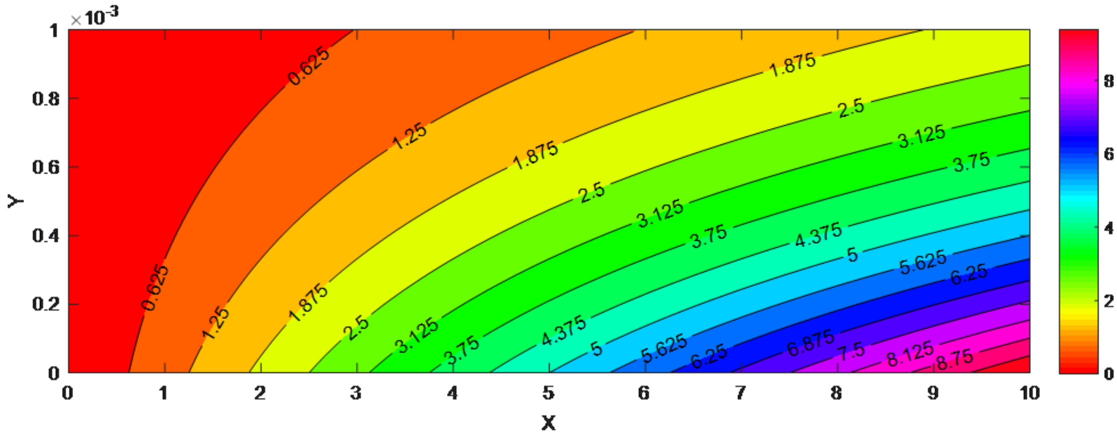

Figure 8. Isotherm of Maxwell ternary nanofluid for $M = 3.1$ at $\alpha = \frac{\pi}{4}$

velocity field decreases, while the temperature field increases with rising values of K. The graphical representation of $'f$ and θ under the physical influence of the radiation parameter is shown in **Figures 19** and **20**, respectively. The graphical results depict that when the radiation parameter is enhanced, both the velocity and temperature fields increase for all three nanofluid cases. However, for the velocity field, the maximum magnitude is observed for Ag / water and the minimum for $Ag-TiO_2-Al_2O_3$ /water, whereas the opposite trend is noted for the temperature field. The effects of the heat generation parameter on velocity and temperature fields for all three nanofluid cases are illustrated in **Figures 21** and **22**. Increasing the heat generation parameter increases the velocity field, while the temperature field decreases rapidly. Finally, the graphical results confirm asymptotic convergence toward the specified boundary conditions, with velocity and temperature profiles exhibiting appropriate asymptotic behavior in all cases.

4.3. Skin friction coefficient and Nusselt number for distinct values of Prandtl parameter

The physical effect of Prandtl number on the skin friction coefficient and Nusselt number is illustrated in **Figures 23** and **24** for nanofluid Ag /water, hybrid nanofluid $Ag-TiO_2$ /water and ternary nanofluid $Ag-TiO_2-Al_2O_3$ /water. The effect of the magnetic number on the skin friction $C_f Re^{1/2}$ and the Nusselt number $Nu\,Re^{-1/2}$, while keeping all other parameters fixed, is presented graphically in **Figure 25** for improved visualization and understanding. The graphical curves for the skin friction coefficient indicate that increasing the Prandtl number increases both the skin friction coefficient and the Nusselt number for all three nanofluid cases. **Figure 25** compares the variations of skin friction and Nusselt number for the simple nanofluid Ag /water, hybrid nanofluid $Ag-TiO_2$ /water, and ternary nanofluid $Ag-TiO_2-Al_2O_3$ /water, respectively. The numerical results for the skin friction and

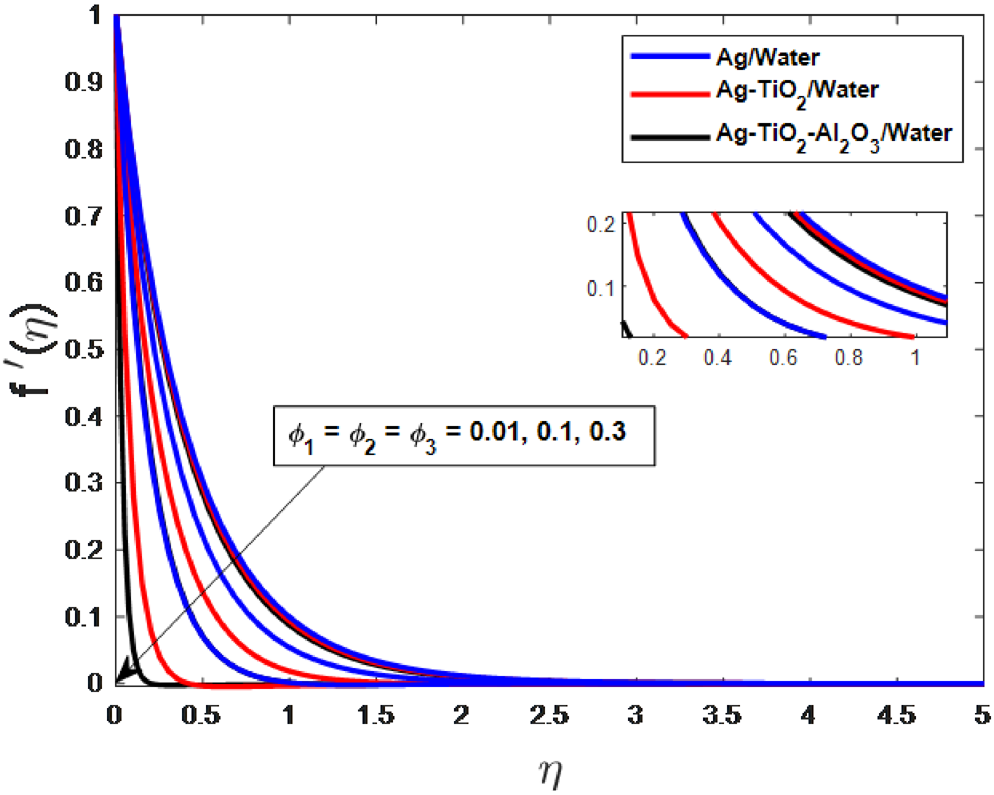

Figure 9. Graphs of $f'(\eta)$ at $\alpha = \frac{\pi}{4}$
Abbreviations: Ag: Silver; Al_2O_3: Alumina; TiO_2: Titania.

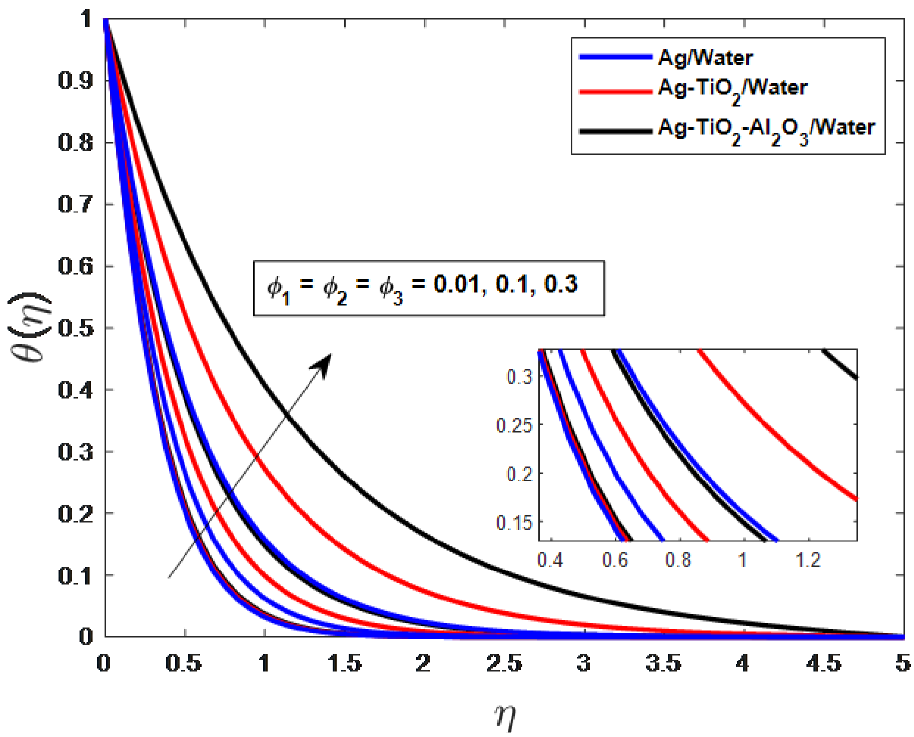

Figure 10. Graphs of $\theta(\eta)$ at $\alpha = \frac{\pi}{4}$
Abbreviations: Ag: Silver; Al_2O_3: Alumina; TiO_2: Titania.

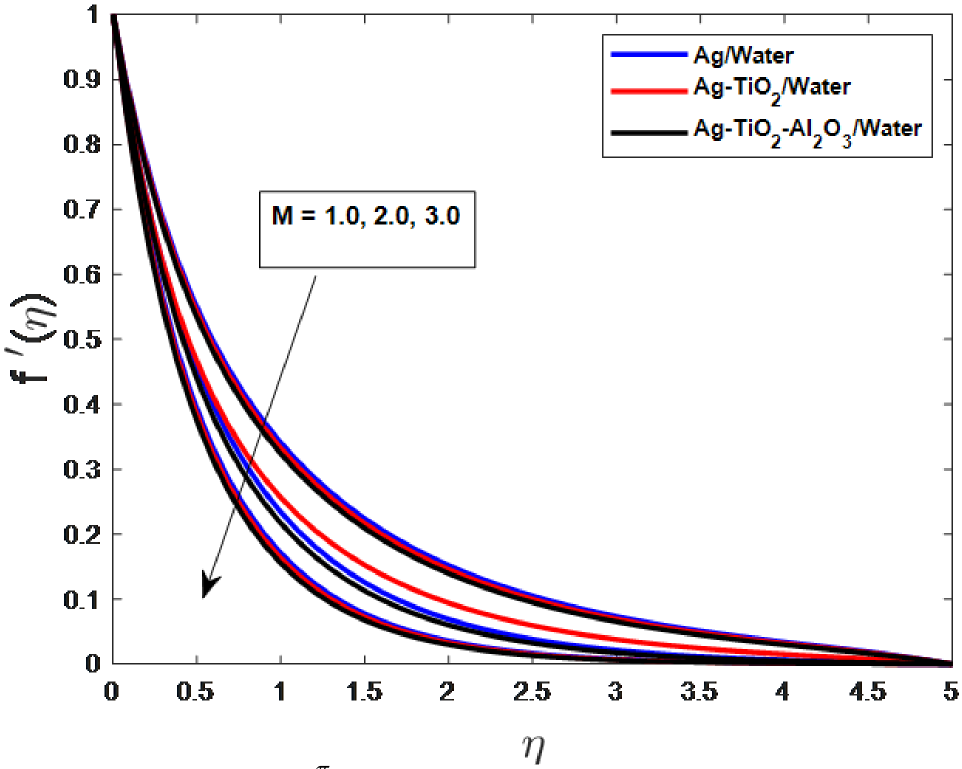

Figure 11. Graphs of $f'(\eta)$ at $\alpha = \frac{\pi}{4}$
Abbreviations: Ag: Silver; Al_2O_3: Alumina; TiO_2: Titania.

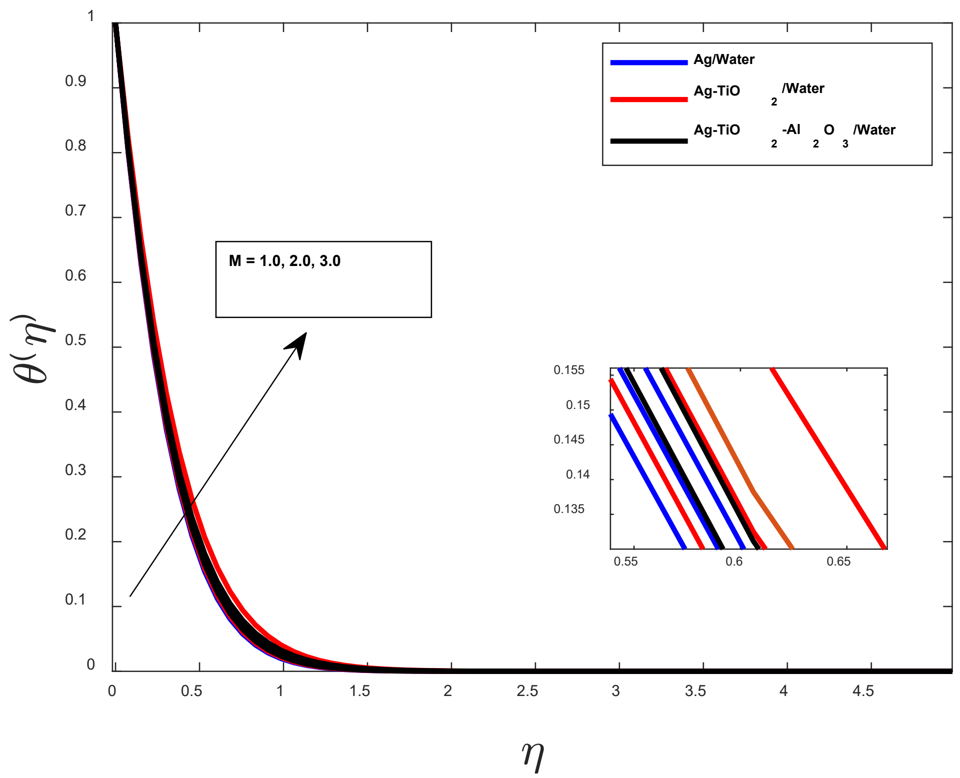

Figure 12. Graphs of $\theta(\eta)$ at $\alpha = \frac{\pi}{4}$
Abbreviations: Ag: Silver; Al_2O_3: Alumina; TiO_2: Titania.

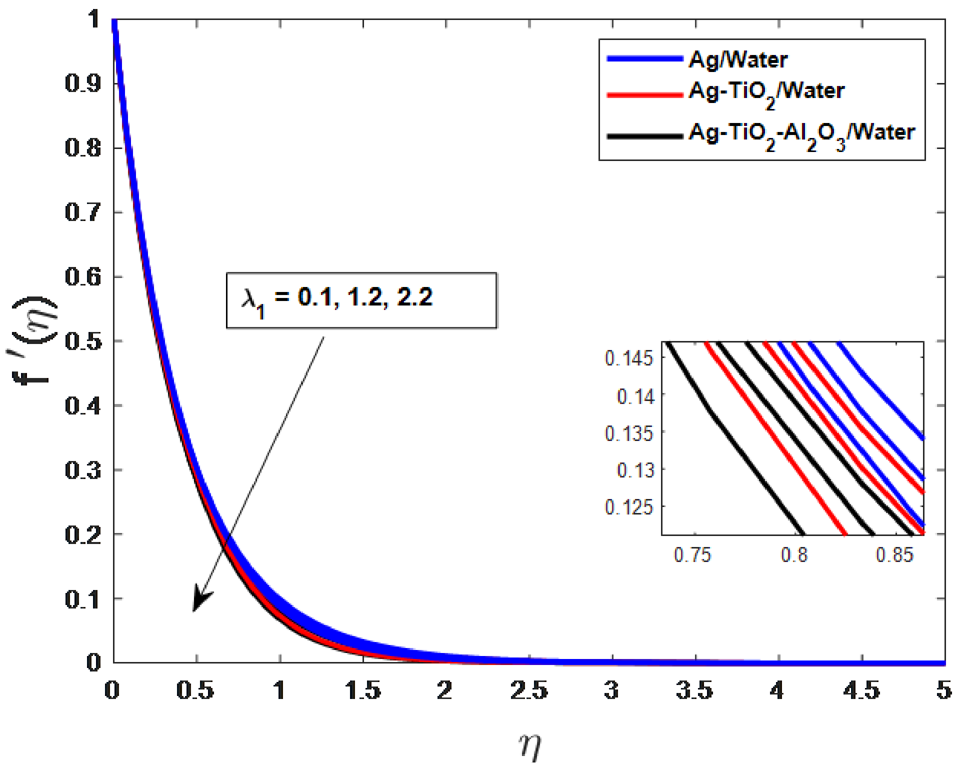

Figure 13. Graphs of $f'(\eta)$ at $\alpha = \frac{\pi}{4}$
Abbreviations: Ag: Silver; Al_2O_3: Alumina; TiO_2: Titania.

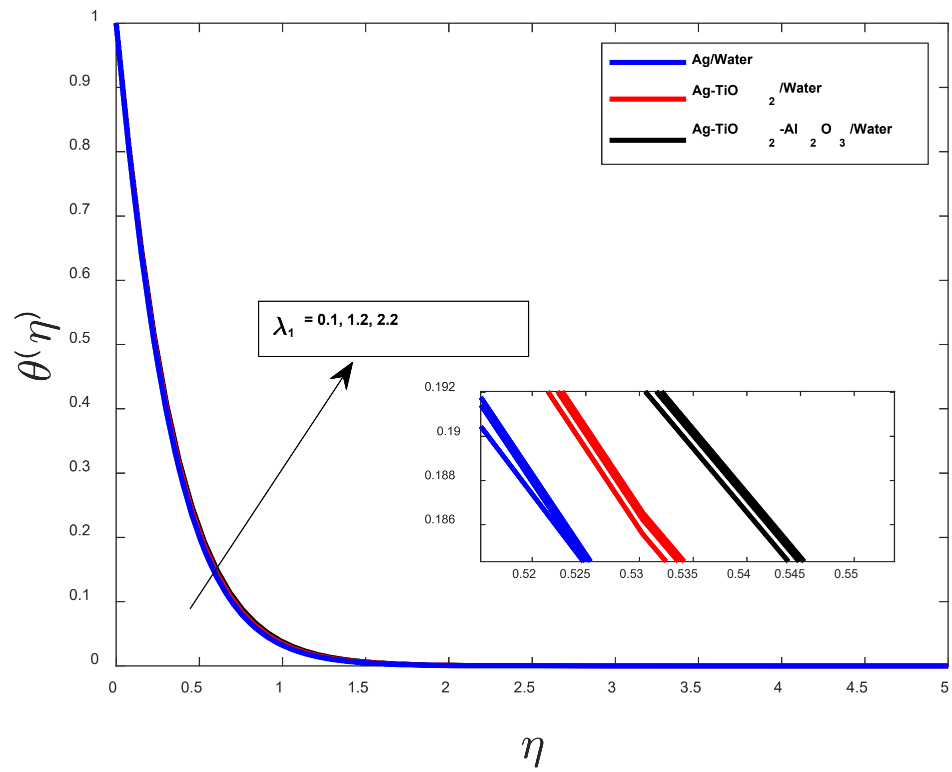

Figure 14. Graphs of $\theta(\eta)$ for at $\alpha = \frac{\pi}{4}$
Abbreviations: Ag: Silver; Al_2O_3: Alumina; TiO_2: Titania.

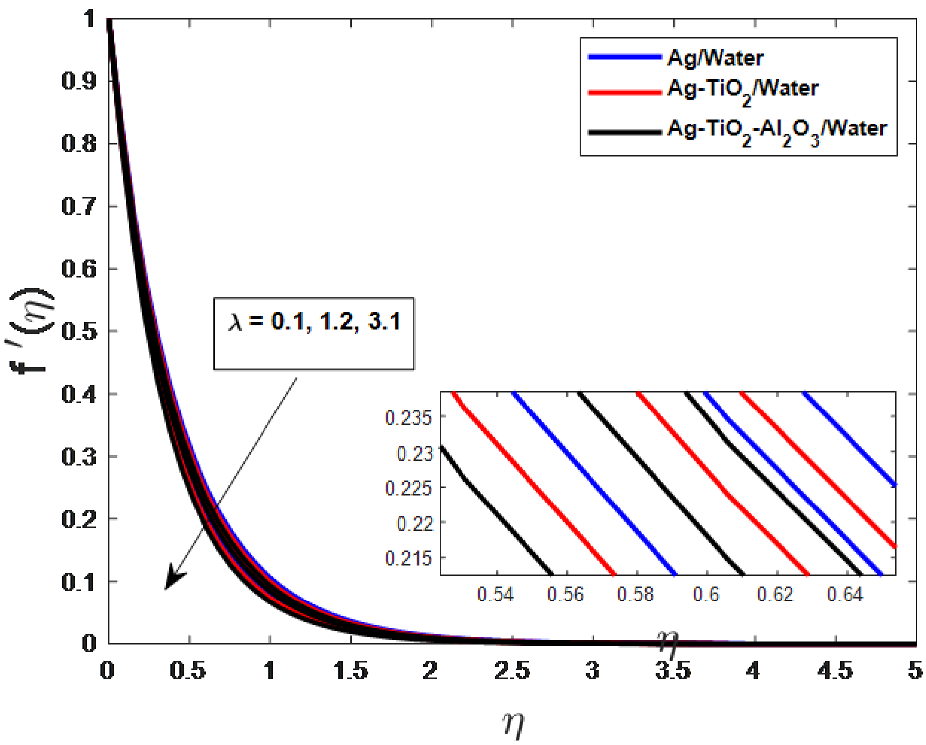

Figure 15. Graphs of $f'(\eta)$ at $\alpha = \frac{\pi}{4}$.
Abbreviations: Ag: Silver; Al_2O_3: Alumina; TiO_2: Titania.

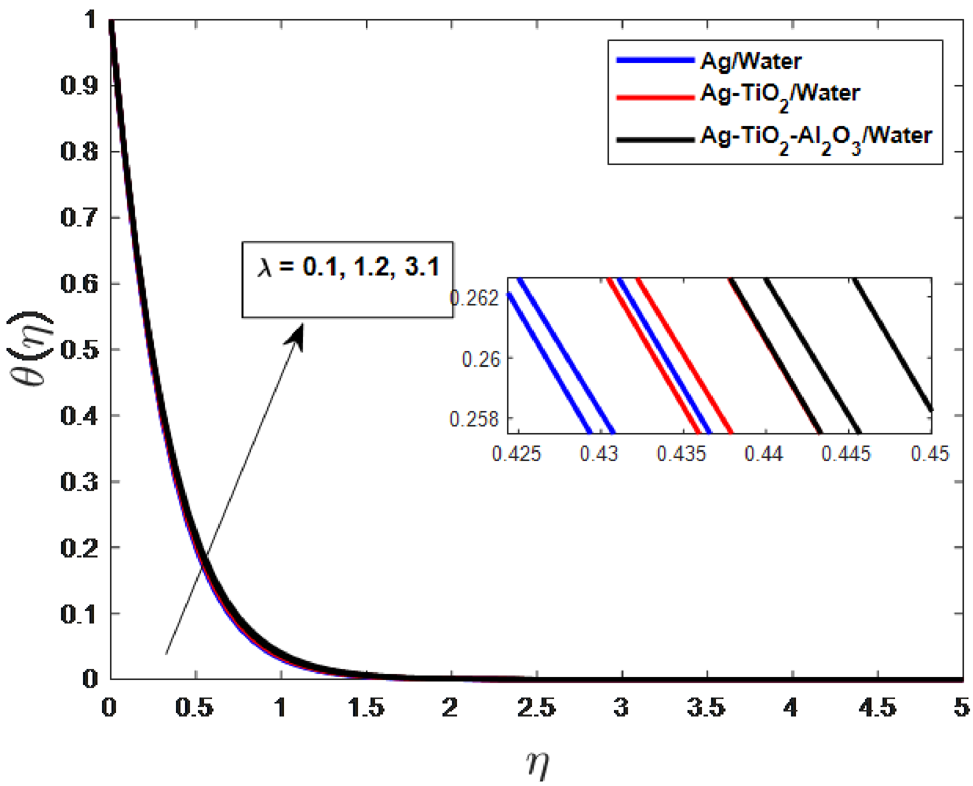

Figure 16. Graphs of $\theta(\eta)$ for at $\alpha = \frac{\pi}{4}$.
Abbreviations: Ag: Silver; Al_2O_3: Alumina; TiO_2: Titania.

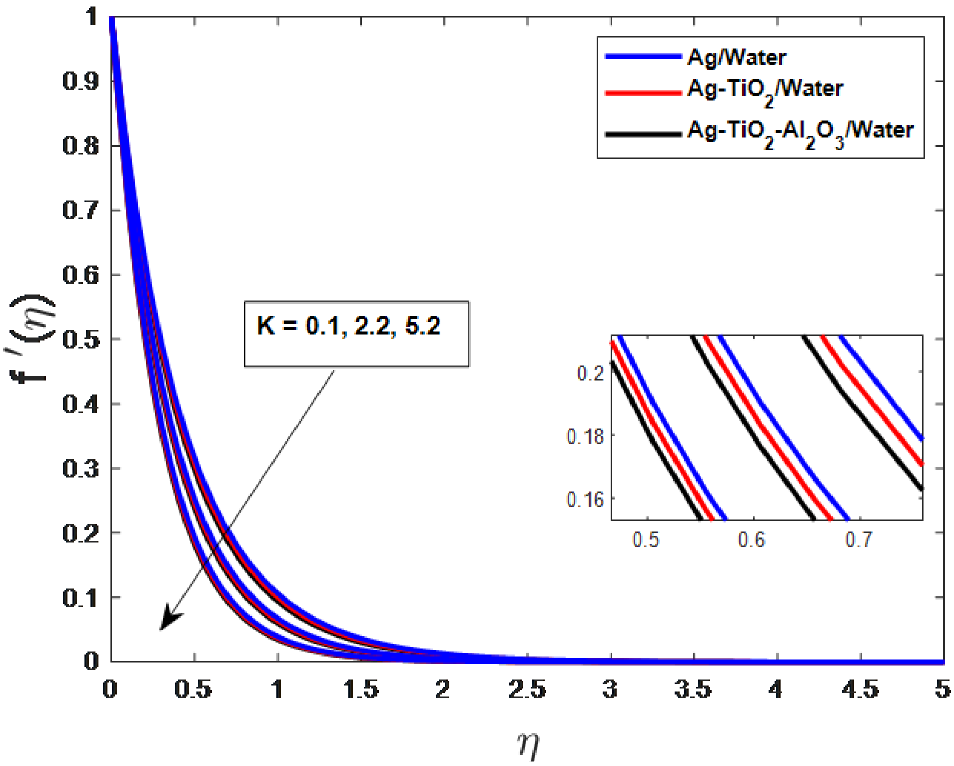

Figure 17. Graphs of $\theta(\eta)$ fat $\alpha = \frac{\pi}{4}$.
Abbreviations: Ag: Silver; Al_2O_3: Alumina; TiO_2: Titania.

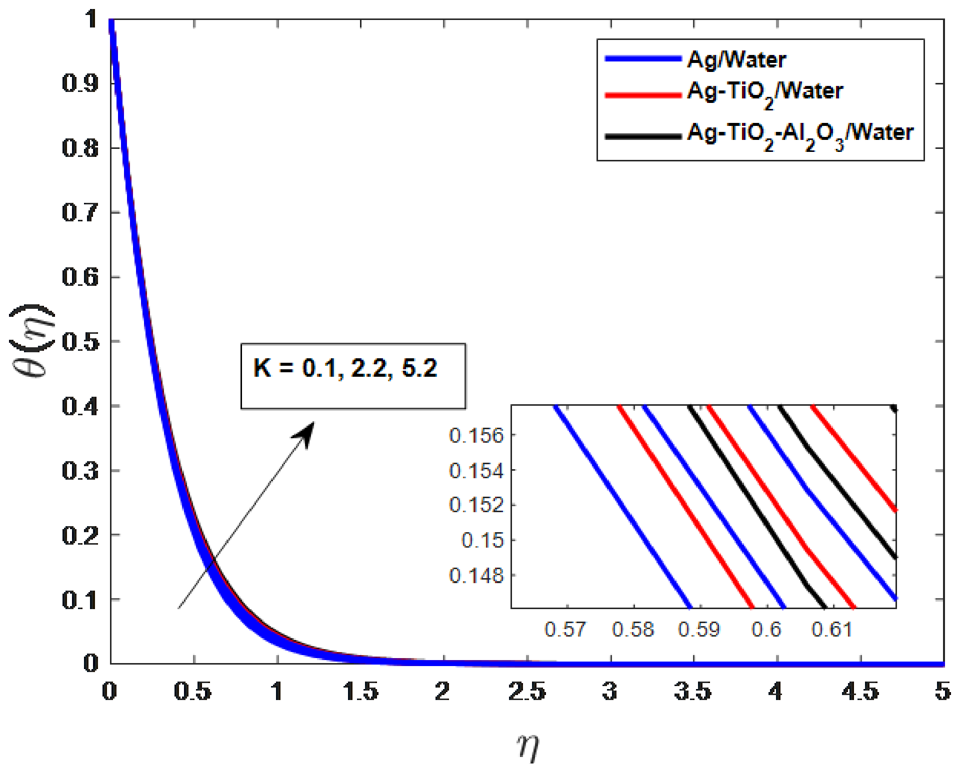

Figure 18. Graphs of $\theta(\eta)$ at $\alpha = \frac{\pi}{4}$.
Abbreviations: Ag: Silver; Al_2O_3: Alumina; TiO_2: Titania.

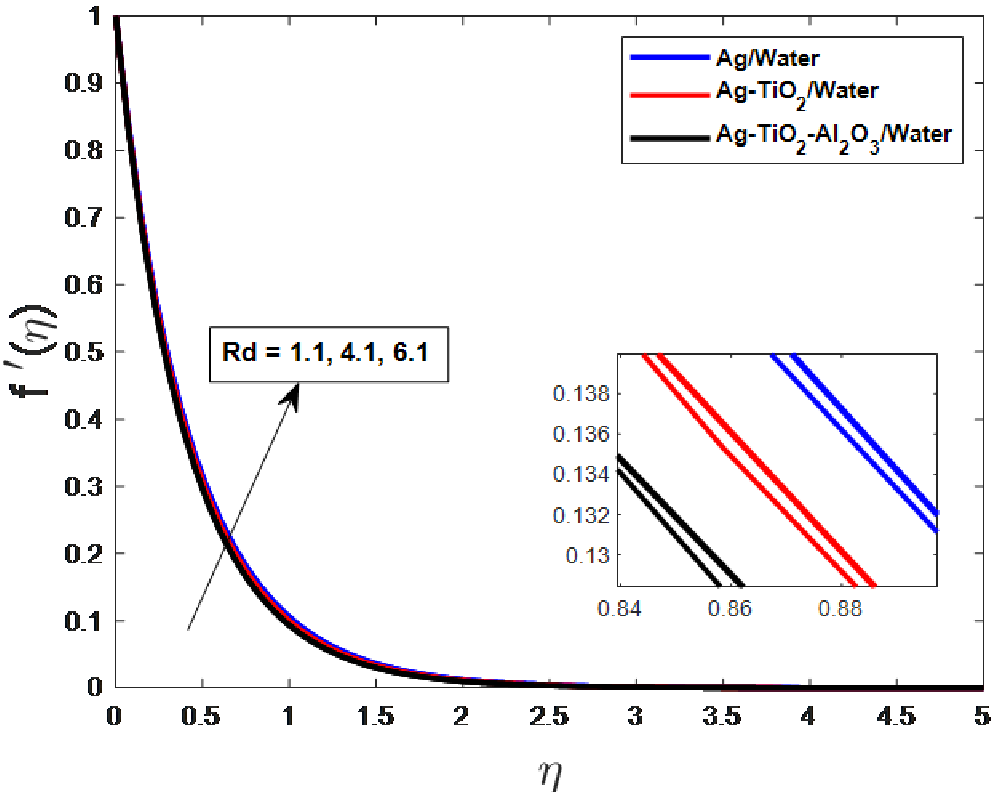

Figure 19. Graphs of $f'(\eta)$ at $\alpha = \dfrac{\pi}{4}$
Abbreviations: Ag: Silver; Al_2O_3: Alumina; TiO_2: Titania.

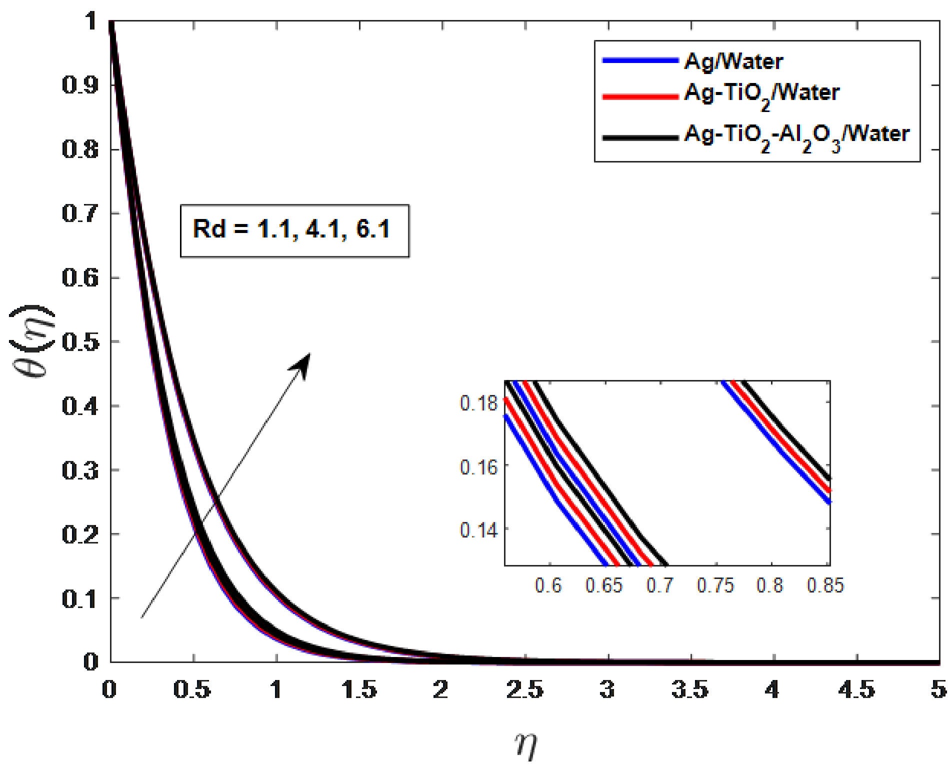

Figure 20. Graphs of $\theta(\eta)$ at $\alpha = \dfrac{\pi}{4}$
Abbreviations: Ag: Silver; Al_2O_3: Alumina; TiO_2: Titania.

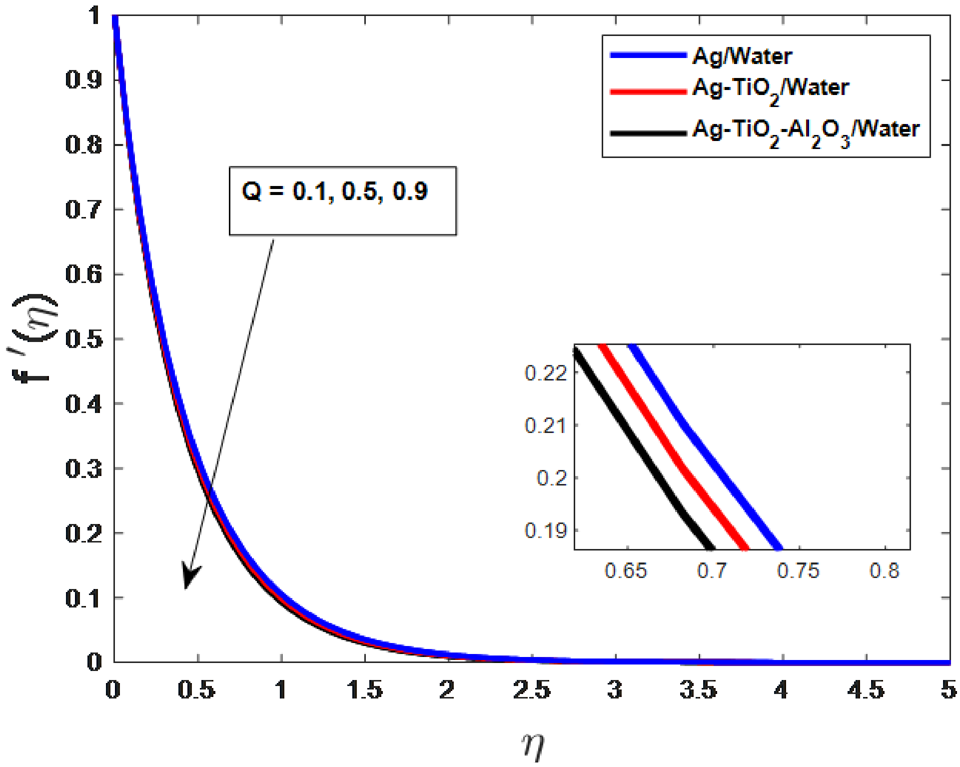

Figure 21. Graphs of $f'(\eta)$ at $\alpha = \frac{\pi}{4}$
Abbreviations: Ag: Silver; Al_2O_3: Alumina; TiO_2: Titania.

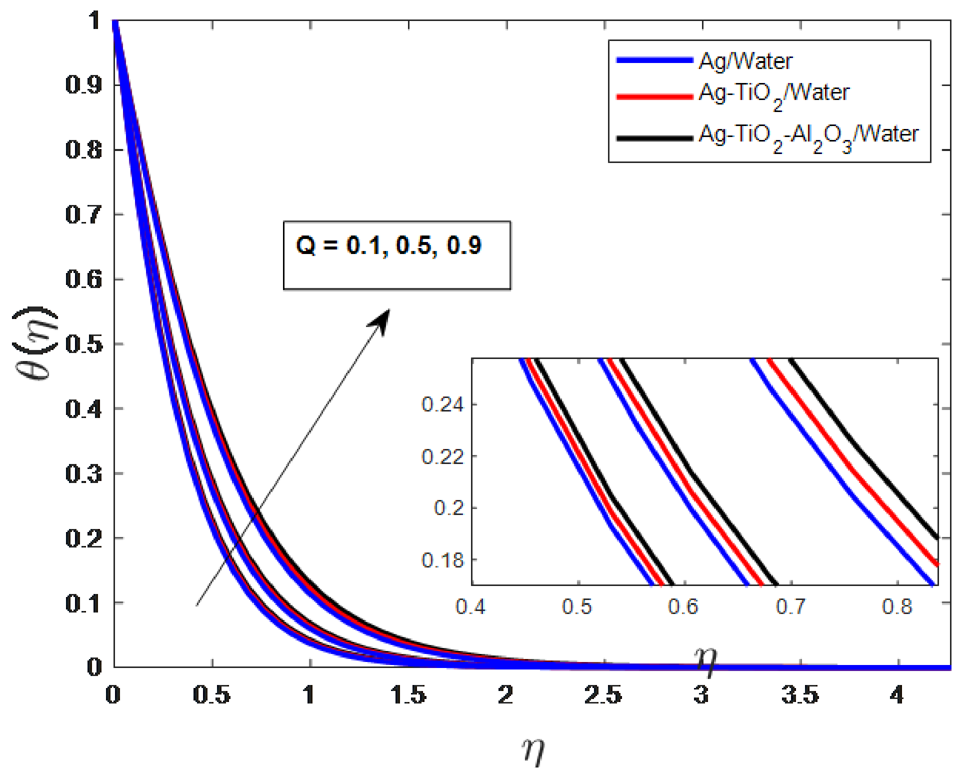

Figure 22. Graphs of $\theta(\eta)$ at $\alpha = \frac{\pi}{4}$
Abbreviations: Ag: Silver; Al_2O_3: Alumina; TiO_2: Titania.

Nusselt number for mono nanofluid Ag /Water are presented in magenta color. It is observed that when the magnetic parameter M increases from 4.1 to 6.1, the skin friction coefficient increases, whereas the Nusselt number decreases gradually. A similar trend is observed for the hybrid nanofluid $Ag-TiO_2$ /water, represented by the purple color, although the overall magnitudes are higher. Likewise, the ternary nanofluid $Ag-TiO_2-Al_2O_3$ /water, represented by the dark green color, exhibits the same qualitative behavior with further enhancement in the results. These findings indicate that the inclusion of additional nanoparticles intensifies the magnetic and thermal transport effects in the flow system.

4.4. Entropy analysis: Entropy generation and Bejan number for distinct values of pertinent parameter

In Entropy analysis, N_G denotes the total entropy production, α_1 represents the temperature ratio, and $Br = Pr.Ec$ is the Brinkman number. **Figure 26** illustrates that an increase in the Brinkman number leads to a significant rise in the total entropy generation. Physically, a higher Brinkman number enhances viscous dissipation, increasing flow resistance and resulting in greater energy loss due to irreversibility. The increase in Br intensifies the pressure drop within the porous medium, requiring additional work to maintain smooth fluid motion and minimize the effect of induced resistance. This additional work performed by the fluid further increases entropy generation, indicating greater thermodynamic irreversibility. The relationship between the Brinkman number and the Bejan number is shown in **Figure 27**. The graphical results show that increasing the Brinkman number decreases the Bejan number. Since the Bejan number quantifies the relative contribution of heat transfer irreversibility to the total entropy generation, the increasing resistance due to the increasing Brinkman number directly affects the Bejan number. Consequently, the system's overall thermodynamic efficiency diminishes. **Figures 28** and **29** show the impact of the magnetic field strength on the entropy generation parameter and the Bejan number. Both parameters exhibit a rising trend with increasing values of

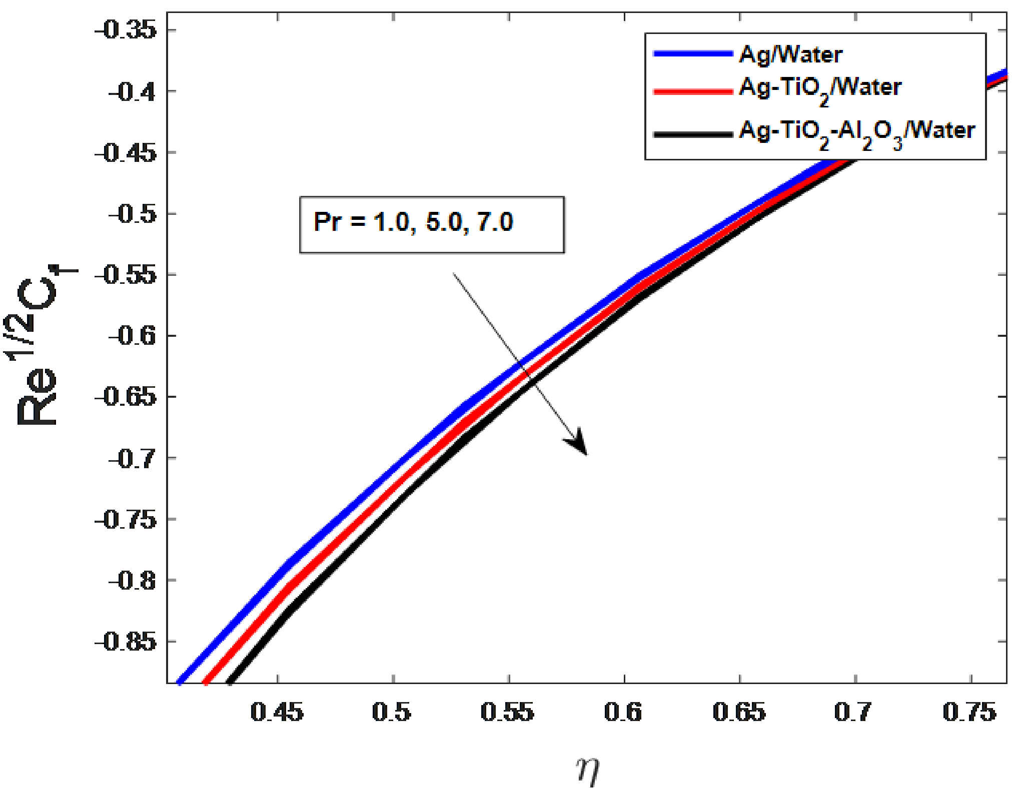

Figure 23. Graphs of $Re^{1/2}C_f$ at $\alpha = \dfrac{\pi}{4}$
Abbreviations: Ag: Silver; Al_2O_3: Alumina; TiO_2: Titania.

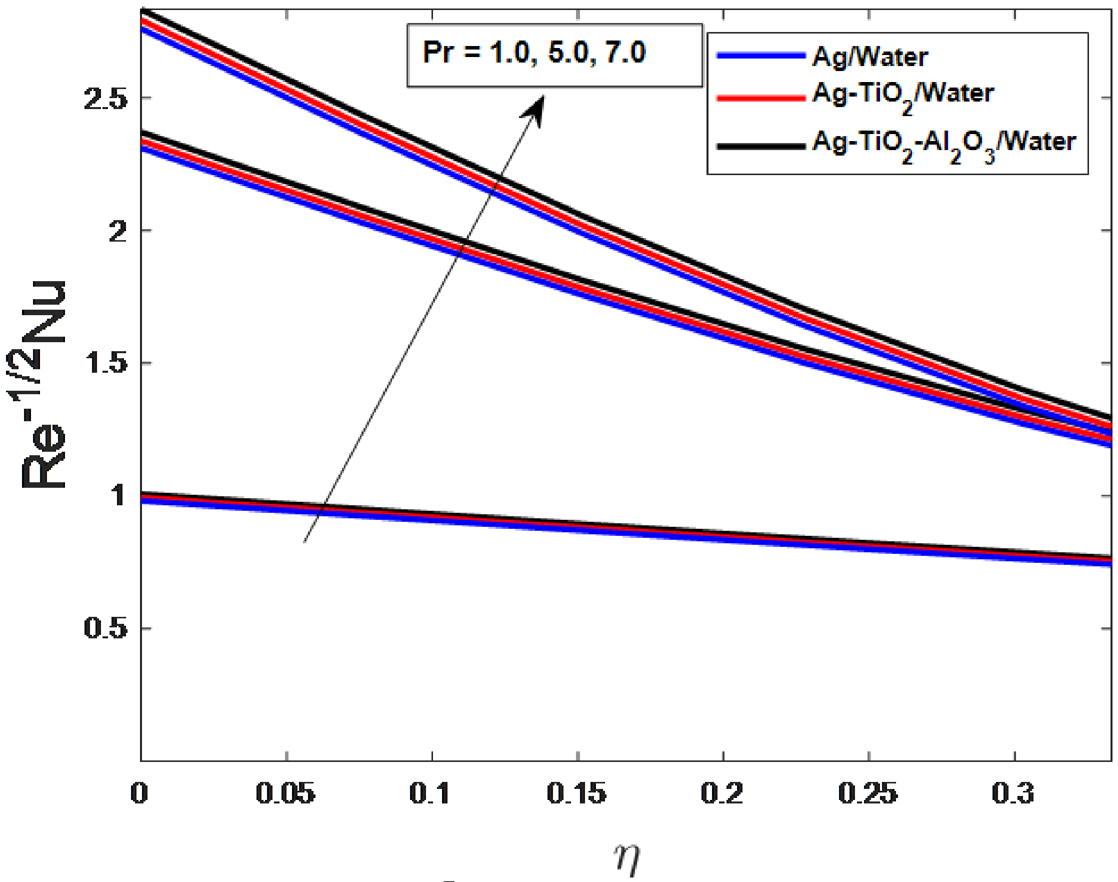

Figure 24. Graphs of $Re^{-1/2}Nu$ at $\alpha = \frac{\pi}{4}$

Abbreviations: Ag: Silver; Al_2O_3: Alumina; TiO_2: Titania.

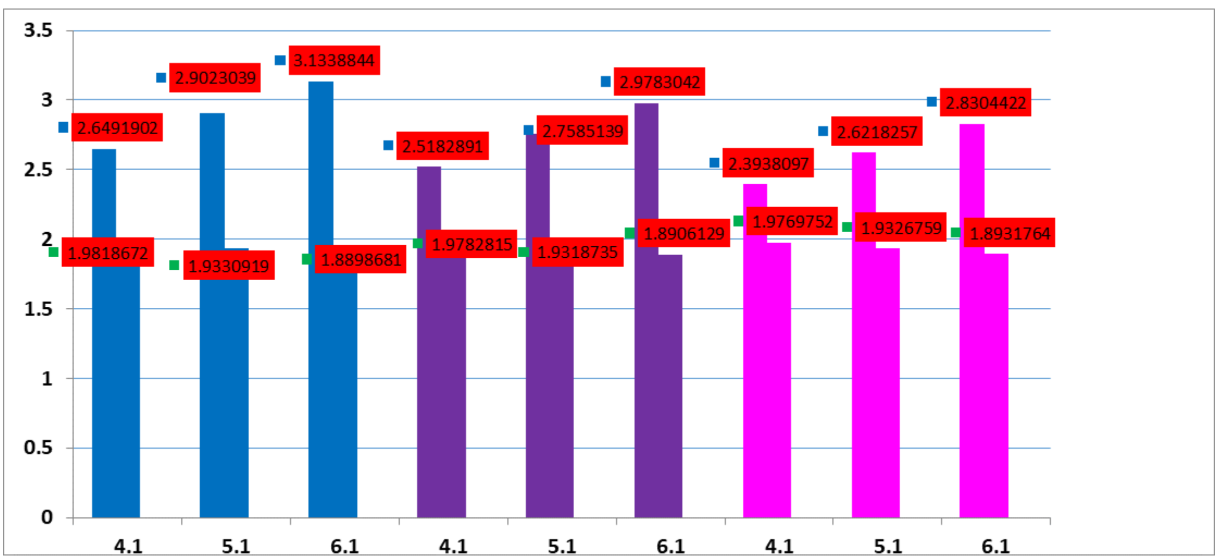

Figure 25. Variations in $C_f Re^{1/2}, Re^{-1/2}Nu$ for $M =$ 5.1; λ_1 = 0.1; K = 0.1; Rd = 5.1; S = 0.1, $\phi_1 = \phi_2 = \phi_3$ = 0.01, λ = 0.9; Q = 0.1, at $\alpha = \frac{\pi}{4}$.

M. All graphical results satisfy the prescribed boundary conditions, confirming the accuracy and consistency of the numerical solutions for all three nanofluid configurations, namely the mono nanofluids, hybrid nanofluid, and ternary nanofluid.

4.5. Comparison of the current results and previously published results for special cases, distinct values

This section presents a comparison between the current findings and previously reported results, with a detailed discussion provided for the special case. The comparison of the current and already published results for the heat transfer rate/reduced Nusselt number is shown in **Table 6**. The present results are in close agreement with the published data, thereby confirming the accuracy and reliability of the current analysis. **Figure 30** presents the tabulated data in graphical form for clearer visualization, revealing excellent consistency between the present study and earlier results for the considered special cases. This strong agreement substantiates the validity of the proposed mathematical model and confirms the effectiveness of the adopted numerical methodology.

Table 6. Comparison of numerical values of $-\theta'(0)$ for various values of Pr when $M = 0.0$; $\lambda_1 = 0.0$; $\lambda = 0.0$; $K = 0.02$; $Rd = 0.0$; $Q = 0.0$; $\phi_1 = \phi_2 = \phi_3 = 0.0$.

Pr	Khan and Pop[31]	$-\theta'(0)$
2.0	0.9113	0.9112
7.0	1.8954	1.8951
20.0	3.3539	3.3537

4.6. Sensitivity analysis

This subsection presents a sensitivity analysis of the Nusselt number with respect to the governing parametric conditions. **Figure 31** illustrates the normalized sensitivity analysis of Nusselt number Nu for the $Ag-TiO_2-Al_2O_3$/water-based ternary nanofluid under different flow equations and governing parameters. The graphical results reveal that the Prandtl number has the greatest influence on heat transfer enhancement, with a normalized sensitivity approaching 0.8. This

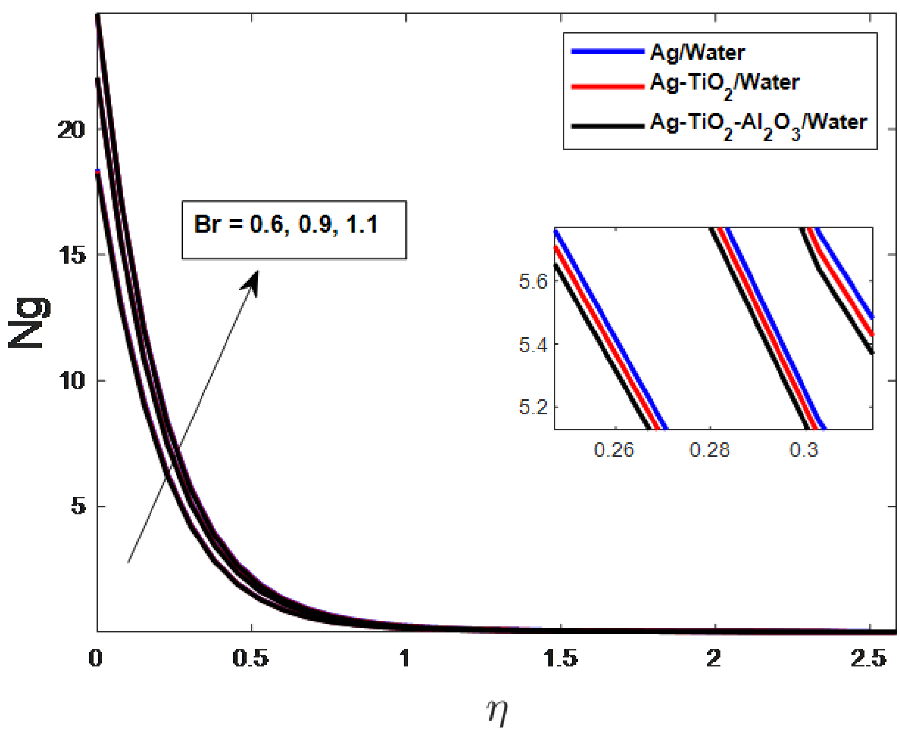

Figure 26. Graphs of total entropy generation at $\alpha = \frac{\pi}{4}$

Abbreviations: Ag: Silver; Al_2O_3: Alumina; TiO_2: Titania.

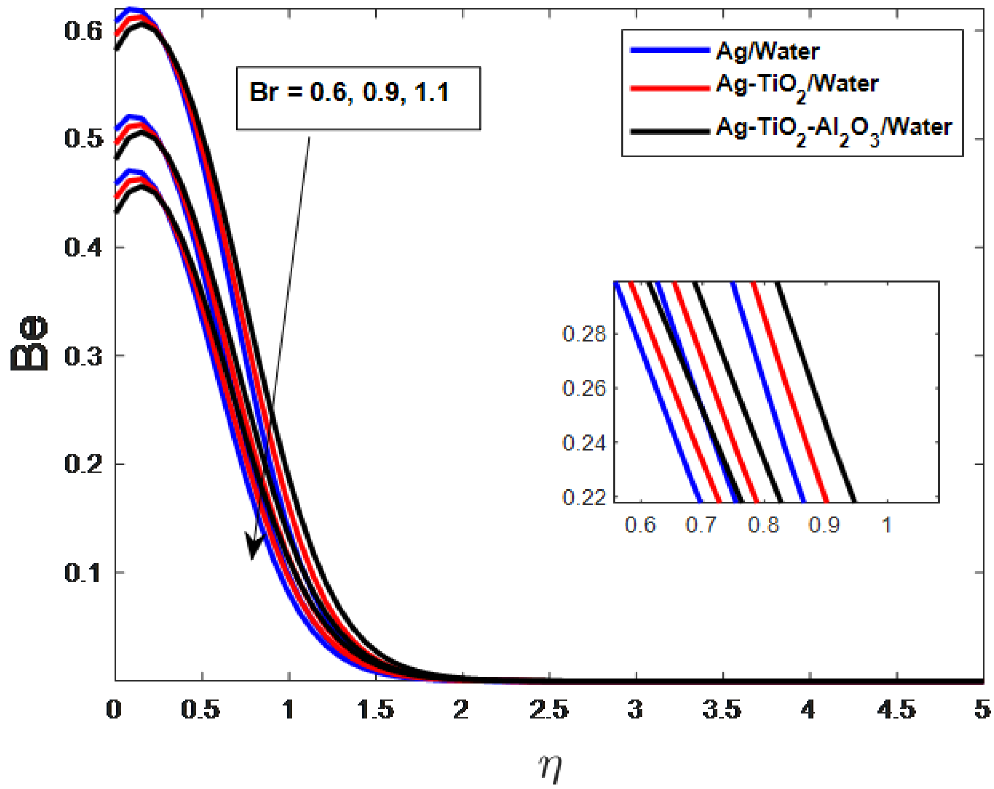

Figure 27. Graphs of Bejan at $\alpha = \frac{\pi}{4}$
Abbreviations: Ag: Silver; Al_2O_3: Alumina; TiO_2: Titania.

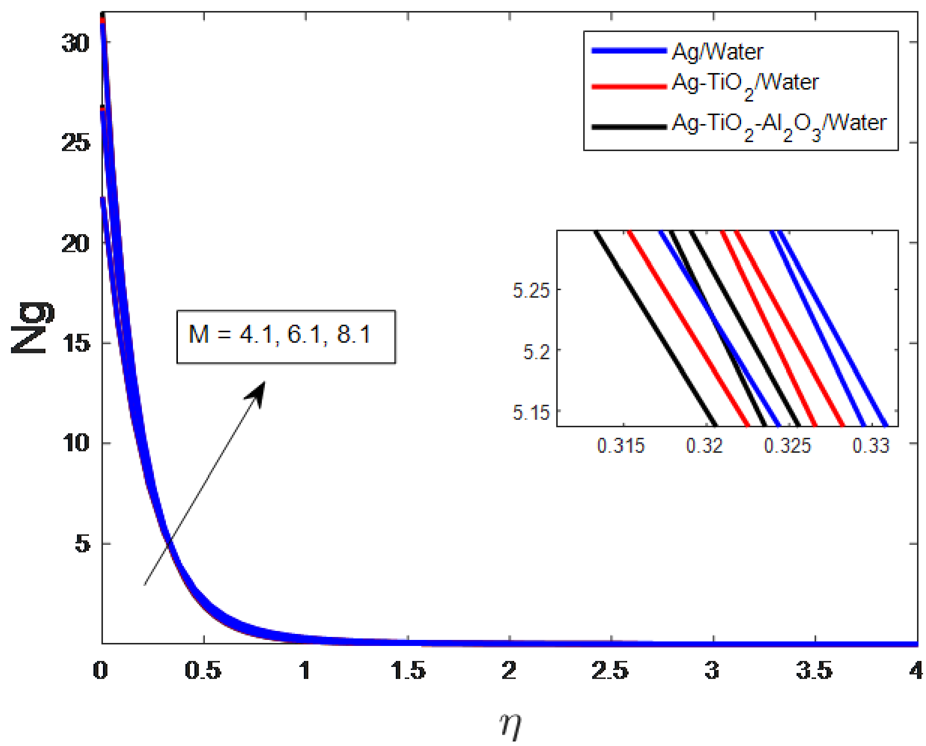

Figure 28. Graphs of total entropy generation at $\alpha = \frac{\pi}{4}$
Abbreviations: Ag: Silver; Al_2O_3: Alumina; TiO_2: Titania.

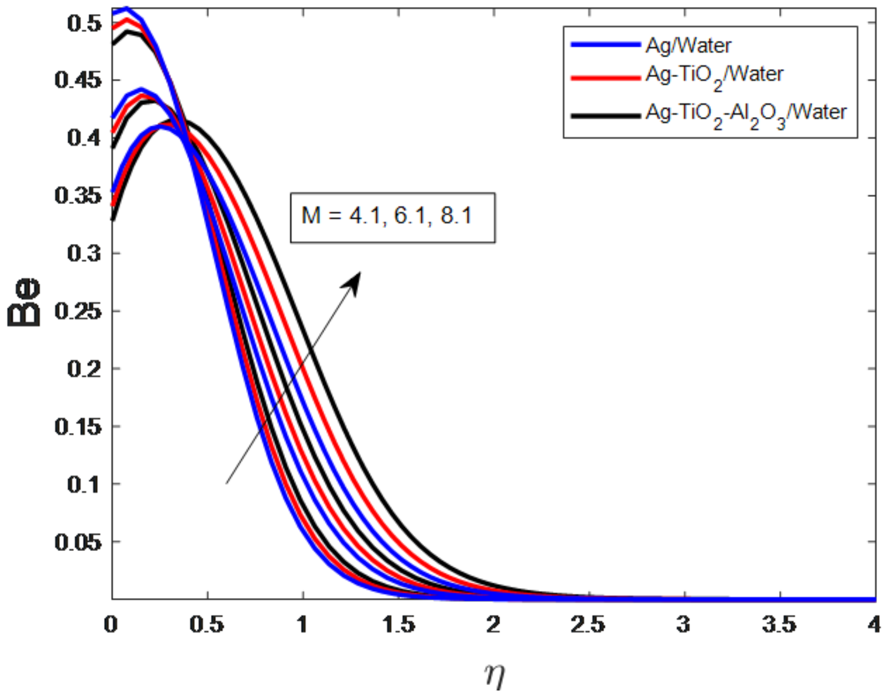

Figure 29. Graphs of Bejan Number at $\alpha = \frac{\pi}{4}$
Abbreviations: Ag: Silver; Al_2O_3: Alumina; TiO_2: Titania.

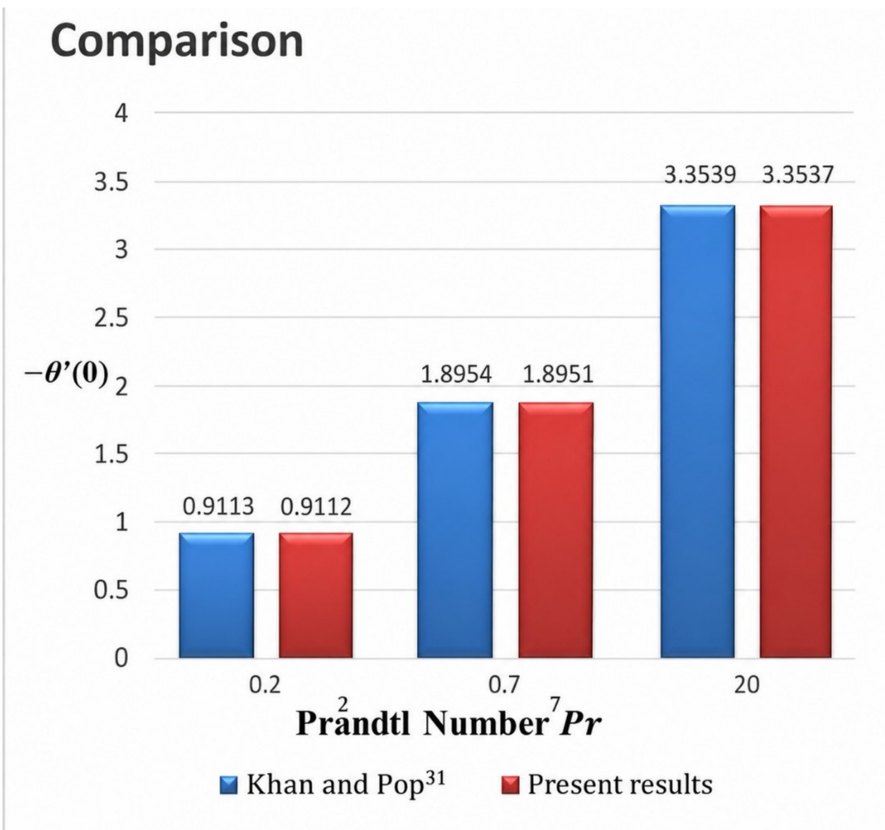

Figure 30. Comparison of numerical values of $-\theta'(0)$ for various values of Pr when Pr when $M = 0.0$; $\lambda_1 = 0.0$; $\lambda = 0.0$; $K = 0.0$; $Rd = 0.0$; $Q = 0.1$; $\phi_1 = \phi_2 = \phi_3 = 0.0$., at $\alpha = \frac{\pi}{2}$

trend indicates that an increase in the Prandtl number strengthens the boundary layer properties and improves the convective heat transfer. The suction parameter also contributes positively by stabilizing the boundary layer and enhancing the surface heat transfer rate. In contrast, the magnetic field parameter shows negative sensitivity, indicating that stronger magnetic forces suppress fluid motion and consequently reduce the heat transfer rate. The radiation parameter shows a moderate positive contribution to the Nusselt number, suggesting that thermal radiation assists energy transportation within the fluid. Conversely, the Maxwell fluid parameter has a negative impact, weakening thermal transport by enhancing fluid elasticity. The nanoparticle volume fractions ϕ_1, ϕ_2, ϕ_3, along with the porous media, Brinkman number, and other associated parameters, exhibit a negative sensitivity, implying a reduction in the heat transfer rate under their increasing influence. Overall, the sensitivity analysis indicates that heat transfer in the ternary nanofluid is strongly influenced by the Prandtl number, magnetic field strength, and suction effects, which play critical roles in optimizing thermal transport performance.

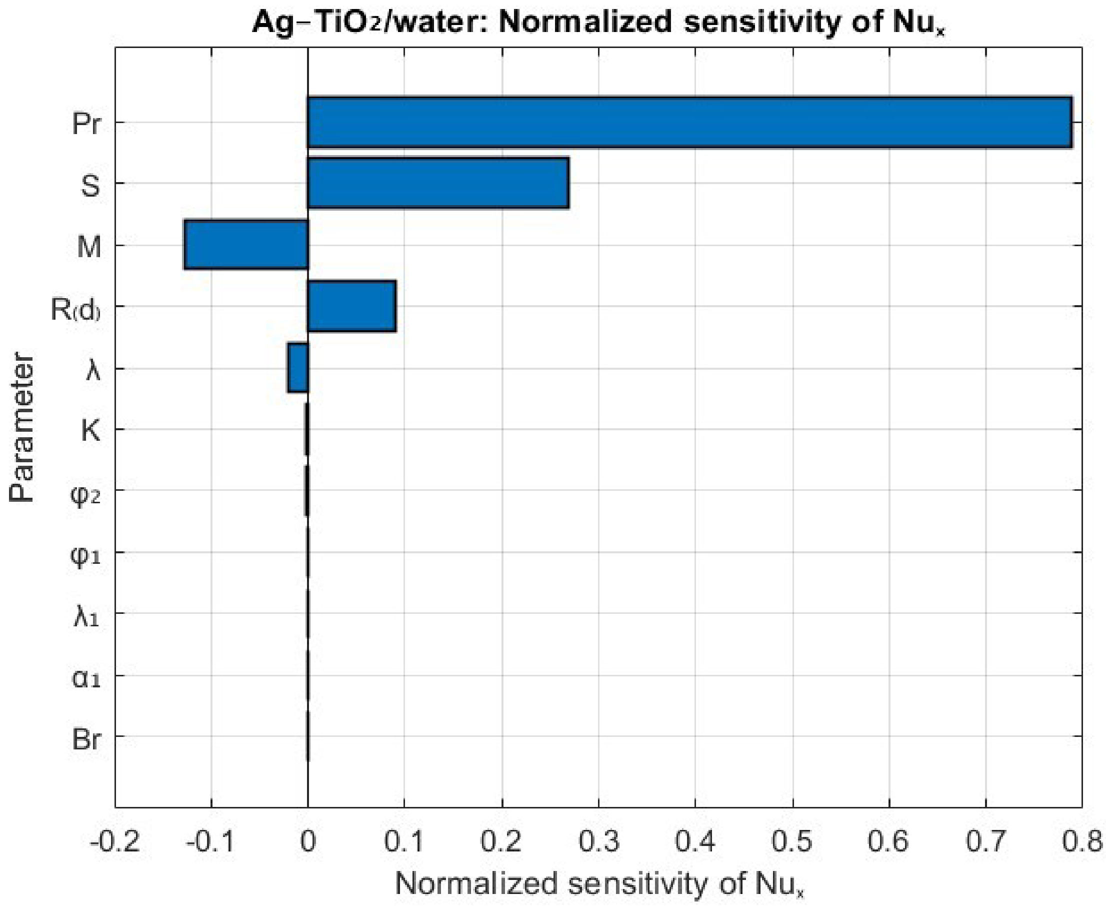

Figure 31. The maximum impact on the heat transfer enhancement
Abbreviations: Ag: Silver; Al_2O_3: Alumina; TiO_2: Titania.

5. Conclusion

In this work, the combined effects of solar radiation and magnetic field on the thermal performance of a ternary nanofluid are investigated within the framework of the Maxwell fluid model. The flow is induced by a stretching inclined surface and accounts for heat generation and porous medium resistance. To further enhance energy efficiency, an entropy generation analysis is also conducted, providing insights into thermodynamic irreversibility within the system.

The main findings of this study are summarized as follows:

- This study demonstrates significant potential

for improving the thermal efficiency of energy conversion systems through the integration of advanced nanofluid modeling and thermodynamic optimization.
- The heat generation parameter has a pronounced effect on enhancing heat energy production.
- It is observed that the total entropy generation increases with increasing Brinkman number.
- An increase in solar thermal radiation and magnetic field parameters enhances the temperature distribution in concentrated solar power systems, potentially increasing thermal power generation efficiency.
- This novel approach creates new opportunities for enhanced thermal management in solar energy systems.
- A numerical model based on the Keller–Box method (finite difference method) for a parabolic trough solar collector involving a stretchable surface, incorporating MHD and ternary nanofluid flow to enhance thermal performance and sustain continuous energy production.
- Increasing solar radiation and magnetic field strength leads to a notable rise in temperature distribution, thereby enhancing thermal energy conversion and overall energy production efficiency.
- A sensitivity analysis is carried out to evaluate and rank the influence of key physical parameters on the system output.
- The validity and accuracy of the present numerical solutions are verified through comparison with previously published studies, demonstrating strong agreement and reliability of the proposed model.

Acknowledgments

None.

Funding

The authors extend their appreciation to the Deanship of Scientific Research at Northern Border University, Arar, KSA, for funding this research work through the project number "NBU-FFR-2026-1902-04."

Conflict of interest

The authors declare they have no competing interests.

Author contributions

Conceptualization: Amir Abbas, Muhammad Farman, Mohamed Ahmed Hafez, Evren Hincal, Betty Wan Niu Voon
Formal analysis: Amir Abbas, Akhlaqur Rahman, Muhammad Farman, Evren Hincal, Sk. A. Shezan, Naveed Ahmad
Investigation: Amir Abbas, Mohamed Ahmed Hafez
Methodology: All authors
Writing – original draft: Amir Abbas, Muhammad Farman, Mohamed Ahmed Hafez, Evren Hincal, Betty Wan Niu Voon
Writing – review & editing: All authors

Availability of data

Not applicable.

AI tools statement

All authors confirm that no AI tools were used in the preparation of this manuscript.

References

1. Manjunatha S, Puneeth V, Gireesha BJ, Chamkha A. Theoretical study of convective heat transfer in ternary nanofluid flowing past a stretching sheet. *J Appl Comput Mech.* 2022;8(4):1279-1286.

   https://doi.org/10.22055/jacm.2021.37698.3067
2. Alshahrani S, Ahammad NA, Bilal M, *et al.* Numerical simulation of ternary nanofluid flow with multiple slip and thermal jump conditions. *Front Energy Res.* 2022;10:967307.

   https://doi.org/10.3389/fenrg.2022.967307
3. Adun H, Adedeji M, Dagbasi M, Bamisile O, Senol M, Kumar R. A numerical and exergy analysis of the effect of ternary nanofluid on performance of photovoltaic thermal collector. *J Therm Anal Calorim.* 2021;145(3):1413-1429.

   https://doi.org/10.1007/s10973-021-10575-y
4. Nasir S, Sirisubtawee S, Juntharee P, Berrouk AS, Mukhtar S, Gul T. Heat transport study of ternary hybrid nanofluid flow under magnetic dipole together with nonlinear thermal radiation. *Appl Nanosci.* 2022;12(9):2777-2788.

   https://doi.org/10.1007/s13204-022-02583-7
5. Arif M, Kumam P, Kumam W, Mostafa Z. Heat transfer analysis of radiator using different shaped nanoparticles water-based ternary hybrid nanofluid with applications: a fractional

model. *Case Stud Therm Eng*. 2022;31:101837.

https://doi.org/10.1016/j.csite.2022.101837

6. Algehyne EA, Alrihieli HF, Bilal M, Saeed A, Weera W. Numerical approach toward ternary hybrid nanofluid flow using variable diffusion and non-Fourier's concept. *ACS Omega*. 2022;7(33):29380-29390.

   https://doi.org/10.1021/acsomega.2c03634

7. Alharbi KAM, Ahmed AES, Ould Sidi M, *et al.* Computational valuation of Darcy ternary-hybrid nanofluid flow across an extending cylinder with induction effects. *Micromachines*. 2022;13(4):588.

   https://doi.org/10.3390/mi13040588

8. Zayan JM, Rasheed AK, John A, *et al.* Synthesis and characterization of novel ternary-hybrid nanoparticles as thermal additives. *Materials*. 2022;16(1):173.

   https://doi.org/10.3390/ma16010173

9. Priyadharshini P, Archana MV, Shah NA, Alshehri MH. Ternary hybrid nanofluid flow emerging on a symmetrically stretching sheet optimization with machine learning prediction scheme. *Symmetry*. 2023;15(6):1225.

   https://doi.org/10.3390/sym15061225

10. Jan SU, Khan U, Abd El-Rahman M, Islam S, Hassan AM, Ullah A. Effect of variable thermal conductivity of ternary hybrid nanofluids over a stretching sheet with convective boundary conditions and magnetic field. *Results Eng*. 2023;20:101531.

    https://doi.org/10.1016/j.rineng.2023.101531

11. Sajjan K, Shah NA, Ahammad NA, Raju CSK, Kumar MD, Weera W. Nonlinear Boussinesq and Rosseland approximations on 3D flow in an interruption of ternary nanoparticles with various shapes of densities and conductivity properties. *AIMS Math*. 2022;7(10):18416-18449.

    https://doi.org/10.3934/math.20221014

12. Sohail M, El-Zahar ER, Mousa AAA, Althobaiti S, Shah NA, Chung JD. Finite element analysis for ternary hybrid nanoparticles on thermal enhancement in pseudo-plastic liquid through porous stretching sheet. *Sci Rep*. 2022;12(1):9219.

    https://doi.org/10.1038/s41598-022-20206-7

13. Ramesh GK, Madhukesh JK, Das R, Shah NA, Yook SJ. Thermodynamic activity of a ternary nanofluid flow passing through a permeable slipped surface with heat source and sink. *Waves Random Complex Media*. 2025;35(2):3499-3519.

    https://doi.org/10.1080/17455030.2022.2053237

14. Faizan M, Ajithkumar M, Reddy MV, *et al.* A theoretical analysis of the ternary hybrid nanofluid with Williamson fluid model. *Ain Shams Eng J*. 2024;15(8):102839.

    https://doi.org/10.1016/j.asej.2024.102839

15. Abbas M, Khan N, Hashmi MS, *et al.* Numerical simulation of Darcy–Forchheimer flow of Casson ternary hybrid nanofluid with melting phenomena and local thermal non-equilibrium effects. *Case Stud Therm Eng*. 2024;60:104694.

    https://doi.org/10.1016/j.csite.2024.104694

16. Farouk B, Shayer H. Natural convection around a heated cylinder in a saturated porous medium. *J Heat Transfer*. 1988;110(3):642-648.

    https://doi.org/10.1115/1.3250540

17. Hossain MA, Vafai K, Khanafer KM. Non-Darcy natural convection heat and mass transfer along a vertical permeable cylinder embedded in a porous medium. *Int J Therm Sci*. 1999;38(10):854-862.

    https://doi.org/10.1016/S1290-0729(99)80040-4

18. Pop I, Na TY. Conjugate free convection over a vertical slender hollow cylinder embedded in a porous medium. *Heat Mass Transf*. 2000;36(5):375-379.

    https://doi.org/10.1007/s002310000124

19. Ullah Z, Alam MM, Khan AA, Alkarni S, Merga FE. Radiative heat and mass transfer of second-grade nanofluid slip flow with variable thermal properties. *AIP Adv*. 2025;15(3).

    https://doi.org/10.1063/5.0254208

20. Salih AA, Ullah Z, Alam MM, *et al.* Turbulent heat and mass transfer in Williamson nanofluid flow over gasketed-plate heat exchanger: Influence of exothermic catalytic-reaction and radiative-heat source. *Eng Sci Technol Int J*. 2026;76:102305.

    https://doi.org/10.1016/j.jestch.2026.102305

21. Riaz MB, Naseer F, Abbas M, Abd El-Rahman M, Nazir T, Chan CK. Solitary wave solutions of Sawada–Kotera equation using two efficient analytical methods. *AIMS Math*. 2023;8(12):31268-31292.

    https://doi.org/10.3934/math.20231601

22. Syed NH, Khan NA, Ahmad N, *et al.* CFD analysis to investigate the effect of inserts on the overall heat transfer coefficient in a concentric tube heat exchanger. *Eng Technol Appl Sci Res*. 2024;14(6):18077-18085.

    https://doi.org/10.48084/etasr.8891

23. Maatki C, Bilal M, Ahmad N, *et al.* Numerical study of three-dimensional unsteady viscous fluid flow across parallel rotating discs with an upward fluctuation and thermal radiation. *J Radiat Res Appl Sci*. 2025;18(2):101577.

    https://doi.org/10.1016/j.jrras.2025.101577

24. Chamkha AJ. Solar radiation assisted natural

convection in uniform porous medium supported by a vertical flat plate. *J Heat Transfer*. 1997;119(1):89-96.

https://doi.org/10.1115/1.2824104

25. Mahendran MS, Wong LS, Dhanapal ACTA, Djearamane S. The effect of titanium dioxide nanoparticles on Haematococcus pluvialis biomass concentration. *J Exp Biol Agric Sci*. 2023;11(2):416-422.

    https://doi.org/10.18006/2023.11(2).416.422

26. Ghasemi SE, Hatami M, Jing D, Ganji DD. Nanoparticles effects on MHD fluid flow over a stretching sheet with solar radiation: a numerical study. *J Mol Liq*. 2016;219:890-896.

    https://doi.org/10.1016/j.molliq.2016.03.065

27. Chen X, Xia XL, Liu H, Li Y, Liu B. Heat transfer analysis of a volumetric solar receiver by coupling the solar radiation transport and internal heat transfer. *Energy Convers Manag*. 2016;114:20-27.

    https://doi.org/10.1016/j.enconman.2016.01.074

28. Pustovalov VK. Modeling and analysis of optical properties of nanoparticles and nanofluids for effective absorption of solar radiation and their heating. *SN Appl Sci*. 2019;1:356.

    https://doi.org/10.1007/s42452-019-0370-2

29. Obalalu AM, Ajala AO, Akindele AO, Oladapo OA, Adepoju O, Jimoh MO. Unsteady squeezed flow and heat transfer of dissipative Casson fluid using optimal homotopy analysis method: an application of solar radiation. *Partial Differ Equ Appl Math*. 2021;4:100146.

    https://doi.org/10.1016/j.padiff.2021.100146

30. Aziz S, Javed R, Nowak A, *et al*. Effects of TiO2, Ag-TiO2, and Cu-TiO2 nanoparticles on mechanical and anticariogenic properties of conventional pit and fissure sealants. *Open Nano*. 2023;14:100185.

    https://doi.org/10.1016/j.onano.2023.100185

31. Khan WA, Pop I. Boundary-layer flow of a nanofluid past a stretching sheet. *Int J Heat Mass Transf*. 2010;53(11-12):2477-2483.

    https://doi.org/10.1016/j.ijheatmasstransfer.2010.01.032

32. Rauf A, Hussain F, Mushtaq A, Shah NA, Ali MR. MHD mixed convection flow for Maxwell hybrid nanofluid with Soret, Dufour and morphology effects. *Arab J Chem*. 2023;16(8):104965.

    https://doi.org/10.1016/j.arabjc.2023.104965

33. Varatharaj K, Tamizharasi R, Vajravelu K. Ternary hybrid nanofluid flow and heat transfer at a permeable stretching sheet with slip boundary conditions. *Eur Phys J Spec Top*. 2025;234:2293-2316.

    https://doi.org/10.1140/epjs/s11734-024-01295-z

34. Devi SA, Devi SSU. Numerical investigation of hydromagnetic hybrid Cu–Al_2O_3/water nanofluid flow over a permeable stretching sheet with suction. *Int J Nonlinear Sci Numer Simul*. 2016;17(5):249-257.

    https://doi.org/10.1515/ijnsns-2016-0037

35. Mukherjee S, Poloju V, Mishra PC. Heat transfer, exergoeconomic performance and sustainability impact of a novel CuO + MgO + GO/water ternary nanofluid. *Appl Therm Eng*. 2023;235:121391.

    https://doi.org/10.1016/j.applthermaleng.2023.121391

36. Aich W, Hussanan A, Abbas A, *et al*. Inclined magnetic field and chemical reaction effects on Maxwell hybrid nanofluid flow in a non-Darcy porous medium. *Z Angew Math Mech*. 2025;105(8):e70172.

    https://doi.org/10.1002/zamm.70172

37. Jameel M, Shah Z, Rooman M, Alshehri MH, Vrinceanu N. Entropy generation analysis on Darcy–Forchheimer Maxwell nanofluid flow past a porous stretching sheet with threshold non-Fourier heat flux model and Joule heating. *Case Stud Therm Eng*. 2023;52:103738.

    https://doi.org/10.1016/j.csite.2023.103738

38. Amudhini M, De P. Irreversibility analysis on tetra-hybrid non-Newtonian fluids with thermal radiation and Soret–Dufour effects over porous inclined stretching sheet. *Results Eng*. 2025;26:104786.

    https://doi.org/10.1016/j.rineng.2025.104786

39. Razzaq A, Hayat T, Khan SA, Razaq A. New concepts of magnetohydrodynamics and entropy rate for radiative nanofluid flow invoking artificial neural network approach. *Results Eng*. 2025;27:106343.

    https://doi.org/10.1016/j.rineng.2025.106343

Amir Abbas *earned his Ph.D degree in Applied Mathematics (Computational Fluid Dynamics and Heat Transfer) in 2021 from the University of Sargodha, Pakistan. He is doing his postdoctoral fellowship at Near East University in Turkey. He is doing an online research fellowship from INTI International University, Nilai, Malaysia. He is working as an Assistant Professor at the Department of Mathematics, Baba Guru Nanak University, Pakistan. He has more than eight years of teaching and research experience. His field of research is computational fluid dynamics and heat transfer. He has published sixty research papers in well-reputed international journals. He has been listed in Stanford University's Top 2% Scientists of 2025 in applied mathematics. His H-index is 31, and his i-10 index is 47. He has produced several MS and MPhil scholars and supervises PhD scholars as well.*
https://orcid.org/0000-0002-3189-1454

Akhlaqur Rahman *received his PhD degree in Electrical and Electronic Engineering from Swinburne University of Technology in 2019. He received his B.Sc in Electrical and Electronic Engineering from American International University-Bangladesh in 2012. Before joining Swinburne, Akhlaqur was a lecturer and coordinator in the Department of Electrical and Electronic Engineering at Uttara University in Bangladesh (2013-2014). Akhlaqur is currently working as a senior lecturer and course coordinator at the Engineering Institute of Technology (EIT). Akhlaqur's research focuses on cloud-networked robotics, machine learning, industrial automation, network optimization, smart manufacturing, and the Internet of Things (IoT).*
https://orcid.org/0000-0002-5491-4436

Muhammad Farman *did Ph.D. Mathematics from the University of Lahore in 2019, Pakistan, and a postdoctoral fellowship from Universitas Airlangga Indonesia, Lebanese American University, and Near East University, North Cyprus, Turkey. He served as an Adjunct Professor (research) at Universitas Airlangga, Indonesia, and the University of Lahore, Pakistan. Currently, he is working as an Associate Professor at Near East University. He has more than eight years of teaching and research experience. The research fields are mathematical biology, control theory, numerical analysis, and the application of fractional calculus to epidemic models. He published more than three hundred research papers in well-reputed SCI and Scopus journals and presented his work at several national and international conferences. He is the recipient of several awards, including the Research Excellence Awards (Best Researcher of the University) in 2019 and 2020 at the University of Lahore. He is ranked among Stanford University's top 2% scientists in applied mathematics for 2023 and 2024. His other achievements include the Best Academic Performance Award 2024, the Publication Honorary Award 2024, and the Most Impactful Researcher Award 2024, all from Near East University, 2024. His H-index is 37, and his i-10 index is 150.*
https://orcid.org/0000-0001-7616-0500

Mohamed Ahmed Hafez *is an accomplished researcher and instructor in civil engineering. He obtained a Bachelor of Science in Civil Engineering from Alexandria University, Egypt. Furthermore, he received a Master of Science focusing on coastal erosion prevention of the Mangrove coastline and a Doctor of Philosophy for his research on ground development of the soft coastal ground from the Universiti of Malaya, Malaysia. He educates and guides aspiring engineers as a lecturer at INTI-IU University in Malaysia. He has accumulated more than three decades of experience in research and consultancy; his expertise primarily lies in coastal reclamation, erosion prevention, ground improvement techniques, slope stability, hydraulic engineering, dam safety, and reservoir sedimentation. After gaining extensive experience in consulting organizations, he transitioned to academia in 2002. He has organized numerous training programs, both domestically and abroad, primarily focused on dam safety management. In addition, he actively participates in the Malaysian National Committee on Large Dams (MYCOLD) and several other Malaysian associations, including the Dam Safety Technical Committee. Furthermore, he is a dam safety expert for numerous consulting companies and associations in Malaysia. Since 2014, he has collaborated with UNITEN R&D and TNB (TNBR). He has written five books primarily focused on soft soil improvement and has collaborated on more than 170 scientific and academic publications published in various magazines, book chapters, and conference proceedings. Furthermore, he has successfully overseen the progress and development of over 30 postgraduate students. In addition, he has been honored with over 25 prestigious national and international gold and silver medals. Notably, he received the WIPO award in 2005 for being the best inventor in water research and geotechnical design from a developing country. His other notable accolades include the Invention Geneva, ITEX Malaysia, and Seoul International Invention awards.*
https://orcid.org/0000-0001-6537-4247

Evren Hincal *was born in Nicosia in 1973. He completed his undergraduate studies at Hacettepe University, Faculty of Science and Letters, Department of Mathematics, and his master's degree with*

honours at Imperial College, University of London, Department of Applied Mathematics. He completed his doctoral studies as a joint project between the Imperial College Biology Department and the Eastern Mediterranean University Mathematics Department. During this period, one of E. Hınçal's doctoral thesis topics, "Investigation of the cancer situation in Northern Cyprus and its evaluation according to European standards," was supported by the Cancer Research Foundation. In 2000 and 2001, E. Hınçal worked on cancer epidemiology as an academic visitor in the Neurobiology Department at Imperial College. Evren Hınçal worked as a part-time lecturer at Eastern Mediterranean and Near East Universities between 1999 and 2006. From 2007 onwards, with the establishment of the Department of Mathematics at Near East University, he became a full-time lecturer in this department. He was promoted to Assistant Professor in 2009, to Associate Professor in 2013, and to Professor in 2019. Since 1998, Evren Hınçal has authored numerous publications in international journals and has participated in many conferences.
https://orcid.org/0000-0001-6175-1455

Betty Wan Niu Voon *obtained a Master's in Science from Universiti Kebangsaan Malaysia. She is a senior lecturer at the College of Engineering, Universiti Tenaga Nasional-Kajang, Kajang, Selangor, Malaysia. Betty Voon Wan Niu is a seasoned mathematics educator with more than 25 years of experience teaching at the undergraduate level. Her skills and expertise include teaching and learning, E-learning, technology-enhanced learning, learning-teaching methods, online learning, online education, chaotic dynamics, and applications. Throughout her career, she has consistently demonstrated a passion for enhancing student learning and engagement through the thoughtful integration of digital tools. She has published several research articles.*
https://orcid.org/0000-0002-7244-2145

Sk. A. Shezan *is an expert in renewable energy integration, power system analysis, power transmission/distribution systems, and power quality analysis. He ranked in the world's Top 2% Scientists (back-to-back 4 years) as listed by Elsevier (in collaboration with Stanford University). He is currently working as an assistant professor in the Department of Electrical Engineering at Northern Border University, Arar, Saudi Arabia; as an adjunct associate professor in the Electrical Engineering Department at Laval University, Canada; and as an adjunct senior lecturer in the School of Energy and Engineering at Murdoch University, Australia. He has also been working at the Engineering Institute of Technology, Melbourne Campus, Australia, as a senior lecturer and unit coordinator, and subsequently at Murdoch University, Perth, Australia. He was an assistant professor in the Electrical and Electronics Engineering Department of the Green University of Bangladesh and a lecturer in the Electrical and Electronics Engineering Department of Uttara University, Dhaka, Bangladesh. Moreover, he previously worked as a grid connection and renewable energy consultant for Doosan GridTech Inc., Melbourne office, Australia, and for Middleton Group as a power system consultant. He completed his PhD degree in Electrical and Electronic Engineering from RMIT University, Melbourne, Australia, in 2021. He received his Master of Engineering degree from the Universiti of Malaya in 2016. Moreover, he received his Bachelor of Engineering degree in Electrical Engineering and Automation from Shenyang University of Chemical Technology, China, in 2013. His research interests and technical expertise lie in microgrid design and analysis, hybrid renewable energy systems, power system modeling and analysis, grid connection studies, feasibility studies, solar energy, wind energy, optimization, control systems, power electronics, BESS monitoring and control techniques, and energy economics.*
https://orcid.org/0000-0003-3636-8977

Naveed Ahmad *is an accomplished assistant professor at the Department of Chemical and Materials Engineering at Northern Border University in Arar, Saudi Arabia. With a Ph.D. from the University of Naples, Federico-II, Dr. Ahmad combines a robust academic foundation with extensive research experience. His expertise spans polymer melt rheology, wastewater treatment, and energy engineering, making him a prominent figure in the field. Throughout his career, he has contributed to numerous high-impact publications and research projects, focusing on innovative solutions for environmental challenges and materials science. Known for his collaborative spirit and dedication to education, Dr. Ahmad plays a vital role in shaping the next generation of engineers. His commitment extends beyond the classroom, as he actively engages in peer review for leading scientific journals and serves as a guest editor for the Energy Engineering Journal. Passionate about advancing sustainable technologies, he is currently involved in groundbreaking research exploring the properties of advanced materials for applications in the energy and environmental sectors. With a diverse skill set and multilingual proficiency, Dr. Ahmad continues to make significant strides in both research and teaching, inspiring students and colleagues alike.*
https://orcid.org/0000-0003-0336-1453

An International Journal of Optimization and Control: Theories & Applications (https://accscience.com/journal/ijocta)